Charm Production with Associated Jets in the Forward Direction at HERA

by **ZLATKA GEORGIEVA STAYKOVA**
from Dobrich, Bulgaria

Diplomarbeit
äquivalente schrift

Hamburg, 2006.

Contents

Introduction

The smallest constituents of matter, besides the leptons, are the constituents of the nucleon, e.g the proton, the *quarks* and *gluons* called *partons*. They have been discovered indirectly in experiments of *deep inelastic scattering* (DIS) where the proton is probed with a lepton. An early model describing the proton structure is the so-called *quark parton model* (QPM) where the proton consists of three partons called quarks. But the first experiments in DIS discovered that only half of the proton momentum is carried by these quarks. In the *quantum chromo dynamics* (QCD) improved QPM, the gluons– the mediators of the strong interaction– contribute to the other half of the proton momentum. The structure of the proton can be described by the *structure function* F_2 which is related to the probability to find a quark or anti quark in the proton at a given scale, the squared momentum transfer in electron proton scattering Q^2.

One of the main purposes of the HERA accelerator and experiments is to measure the structure functions of the proton. HERA collides electrons and protons at a center of mass energy of $\sqrt{s} \approx 318\,\mathrm{GeV}$. At such high energies the squared momentum transfer can be very large ($Q^2 \approx s \approx 90000\,\mathrm{GeV}^2$). At the same time the variable x, which can be interpreted as the fraction of the proton momentum carried by the struck quark in the QPM, can reach extremely low values. It was a big surprise in the first measurements at HERA to observe that the structure function rises strongly towards small values of x. In this region of phase space the behavior of the structure function is controlled mainly by gluon splitting. However, at some low value of x one expects this to turn over and the opposite process (*recombination of gluons*) to dominate. At the present accelerators this phenomenon is under intensive investigation.

The description of the partonic structure of the proton is approximated within different theoretical QCD models by so-called *evolution equations*. They give the probability that the scattered parton emits or splits into new partons. These evolutions are performed in terms of virtualities of the partons (DGLAP) or momentum fractions (BFKL). Both models are applicable in

different regions of phase space– DGLAP for moderate and high values of x and BFKL for small values of x. A unification of both models is implemented in the CCFM evolution approach. However, the structure function does not provide any information of the parton ladder itself, but only of the cross section. Therefore exclusive quantities have to be considered e.g *jets*, particle production and energy flow.

When a hadronic jet is found in the direction of the proton, so–called *forward jet*, it is very likely that it originates from a parton that was radiated early in the evolution ladder. Therefore by studying forward jets, one can select events where many partons are emitted and the evolution ladder is long enough to possibly differentiate between the parton evolution schemes. Additional requirements on the jets can be made in order to enhance the phase space which is most sensitive to different parton dynamics. With the selection of charm events one can reach the lowest possible values of the momentum fraction x.

The study of parton evolution at low x is very important for the future experiments at the LHC where $x \sim 10^{-7}$ possibly will be reached.

The thesis is organized as follows:
In the first chapter, the basic foundations of the QCD theory are given. The different evolution models are briefly discussed. The layout of the HERA machine and the H1 detector is described in chapter 2. Monte Carlo (MC) studies on D^* meson with an associated jet at central rapidities in photoproduction are presented in chapter 3. Parton level studies on forward jet physics in the presence of a charm quark in DIS are shown in chapter 4. Correlations between forward jets and charm quarks and mesons in photoproduction are treated in chapter 5. Finally, in chapter 6 a pre study of D^* and forward jets using data measured by the H1 detector, is presented.

Chapter 1

Deep Inelastic Scattering and Photoproduction

In this chapter the basic foundations of the theory of inelastic electron-proton scattering are presented. The first section presents the underlying kinematic variables. The fact that the proton is not a point-like object arises the need of *parton density functions*– discussed in section 1.2. Photoproduction of heavy quarks is briefly described in 1.3. In the next section 1.4 Monte Carlo event generators– the standard tools used in experimental high energy physics, are discussed. Finally jet production is described in 1.5.

1.1 DIS Kinematics

At HERA, beams of electrons (or positrons) with an energy of $E_e = 27.6\,\mathrm{GeV}$ collide with protons with an energy of $E_p = 920\,\mathrm{GeV}$. The electron probes the proton via exchanging a Z^0 boson in *neutral current* (NC) processes or a photon in *electromagnetic processes* (EM):

$$e^- + p \longrightarrow e^- + X \tag{1.1}$$

The exchanged boson can also be a charged $W^{\pm}$. The resulting process is called *charged current* (CC) process:

$$e^- + p \longrightarrow \nu_e + X \tag{1.2}$$

The possible processes in ep scattering are shown in figure 1.1.

With the four-momentum of the proton $P = (E_p, \mathbf{p_p})$, the incoming electron $k = (E_e, \mathbf{k_e})$ and the outgoing electron $k' = (E_{e'}, \mathbf{k_{e'}})$, one can define the following Lorenz invariant variables:

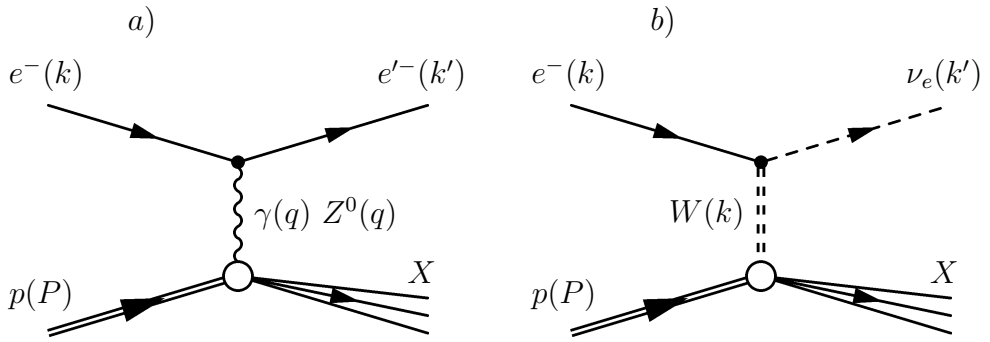

Figure 1.1: *Neutral current and electromagnetic process a) and Charged current process b)*

$$Q^2 \equiv -q^2 = -(k - k')^2 \tag{1.3}$$

where q is the four-momentum of the exchanged virtual boson. The squared momentum transfer may be considered as the invariant mass squared of the exchanged boson[1]. If $Q^2 \ll 1000\,\mathrm{GeV}^2$ events with Z^0 and $W^\pm$ can be neglected due to their large masses ($M_W = 80.4\,\mathrm{GeV}$,$M_Z = 91.2\,\mathrm{GeV}$). The regime of small virtuality (Q^2<1 GeV) is called *photoproduction* and the regime of large Q^2, *deep inelastic scattering* (DIS). Photoproduction events are usually selected with a cut of $Q^2 < 1\,\mathrm{GeV}^2$, DIS events with $Q^2 > 1\,\mathrm{GeV}^2$.

The invariant mass squared (W^2) of the photon-proton system,

$$W^2 = (P + q)^2 \tag{1.4}$$

is equivalent to the invariant mass squared of the hadronic system in the final state.

In the elastic scattering process, the proton remains intact, $X \equiv p$. When inelastic scattering occurs, X is the Hadronic Final State (HFS) with mass W, created from the photon-proton interaction. In this case the invariant mass of the HFS is much larger than the proton rest mass ($W^2 \gg m_p^2$), the proton splits up completely and the process is called DIS.

The variable $s = (k + P)^2$ is the center-of-mass energy squared. For HERA the center-of-mass energy is $\sqrt{s} = 318.7\,\mathrm{GeV}$.

The following variables (*Bjoerken* variables) are used to describe the DIS processes:

[1]Often, the variable Q^2 is referred to as *virtuality* of the exchanged boson.

$$x_{Bj} = \frac{Q^2}{2P \cdot k} \tag{1.5}$$

$$y = \frac{P \cdot q}{P \cdot k} \tag{1.6}$$

In the *Quark Parton Model* (QPM), x_{Bj} is the fraction of the proton momentum carried by the scattering parton. The fractional energy lost by the lepton in the collision is given by the inelasticity of the scattered electron y. In the proton rest frame, it is the fraction of the leptons momentum carried by the photon.

However, not all of these variables are independent. Neglecting the masses of the electron and the proton, Q^2 and W are related to x_{Bj}, y and s via the following equations:

$$Q^2 = xys \tag{1.7}$$

$$W^2 = ys - Q^2 \tag{1.8}$$

In inclusive scattering, at a fixed value of s, two of these variables are independent, for example x_{Bj} and Q^2, which can be calculated from scattered electron and the HFS.

Rapidity

For the final state objects the *rapidity*[2] y, is defined with the following expression:

$$y = \frac{1}{2} \ln \frac{E + p_z}{E - p_z} = \frac{1}{2} \ln \frac{(E + p_z)^2}{m^2 + p_t^2}$$

where E and p_z are the energy and the z component of the momentum, respectively. In very high energies one can neglect the masses of the particles and thereby define the *pseudorapidity*:

$$\eta = y|_{m=0} = -\ln(\tan \frac{\theta}{2}) \tag{1.9}$$

where θ is the polar angle of a particle[3].

The rapidity can be related to the momentum fraction of a parton, shown in appendix A.

[2]Not the Bjoerken y!

[3]Defined this way the pseudorapidity is positive in the proton direction and negative in the electron direction

1.2 The Structure of the Proton and Evolution Equations

1.2.1 Structure Functions

For inclusive *ep*-scattering, the double differential cross section for a EM process is given by *Quantum Electro Dynamics* (QED) if the parameters $F_{1/2}$ are known:

$$\frac{d\sigma(e^{\pm}+p\rightarrow e^{\pm}+X)}{dxdQ^2}=\frac{4\pi\alpha_{em}^2}{xQ^4}\cdot\left(xy^2F_1(x,Q^2)+(1-y)F_2(x,Q^2)\right) \quad (1.10)$$

where α_{em} is the electromagnetic constant and $F_{1/2}(x)$ are the proton *structure functions*. The structure functions can be expressed in terms of the *parton densities* $f_q(x)$ and $f_{\overline{q}}(x)$ which give the probability to find quark (or anti-quark) with a momentum x_i at a scale Q^2 in the proton:

$$F_2(x)=x\sum_q e_q^2\left(f_q(x,Q^2)+f_{\overline{q}}(x,Q^2)\right) \quad (1.11)$$

where e_q is the electric charge of the parton.

In the QPM the proton consists of pointlike fermions– called partons. These *valence quarks* carry approximately one third of the proton momentum. The electron scatters directly on one one of them:

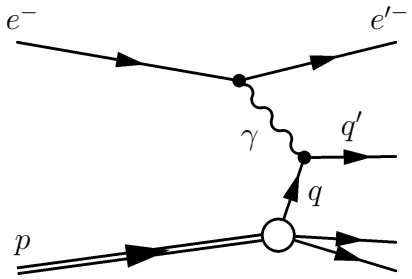

Figure 1.2: *QPM process, zeroth order* α_s *. The electron scatters on valence quark.*

As a consequence, the parton density functions and the structure functions of the proton become independent of Q^2, a phenomenon known as *Bjoerken scaling* which is violated in *quantum chromo dynamics* (QCD). At fixed values of x_{Bj} one originally observed that $F_2(x,Q^2)$ is nearly independent of Q^2 which helped establish the QPM [1]:

$$F_i(x, Q^2) \approx F_i(x), \quad i = 1, 2 \tag{1.12}$$

Moreover the Callan-Gross relation between F_1 and F_2 is:

$$F_2(x) = 2xF_1(x) \tag{1.13}$$

This is true only if the induced parton is a fermion, as in the QPM.

Finally the double differential cross section for NC processes can be written:

$$\frac{d\sigma(e^{\pm} + p \to e^{\pm} + X)}{dxdQ^2} = \frac{4\pi\alpha_{em}^2}{xQ^4} \cdot \left(2(1-y) + y^2\right) \cdot F_2(x) \tag{1.14}$$

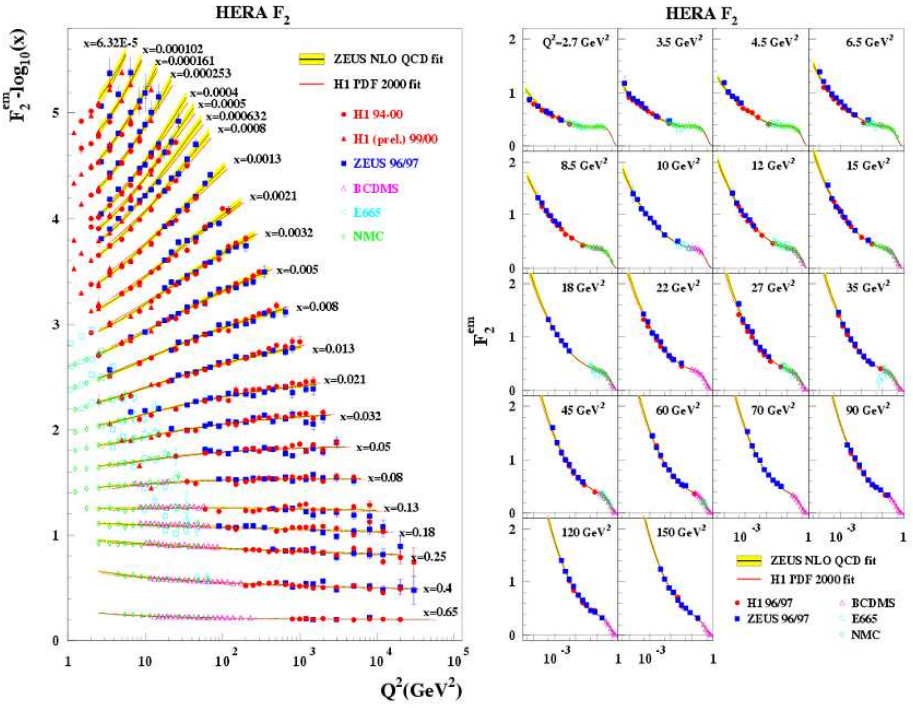

Figure 1.3: *Measurements made by H1 and ZEUS at the HERA accelerator, the structure functions F_2 as a function of Q^2 (left) and as a function of x_{Bj} for different values of Q^2 (right)*

Increasing the momentum transfer Q^2, the photon can probe smaller distances and is able to resolve the scattered parton into a parton and a gluon, or the splitting of a gluon into a quark anti-quark pair. The QPM does not take into account these processes, QCD is needed to improve the QPM.

Thus, some qualitative changes in parton distributions are needed– gluon bremsstrahlung will shift the valence and sea distributions to smaller x_{Bj}, and the gluon splitting will increase the amount of sea quarks. The measurements of the structure function F_2 made by H1 and ZEUS are shown in figure 1.3.

At relatively high values of x_{Bj} the structure function exhibit flat behavior with increasing Q^2 (Bjoerken scaling). The smaller x_{Bj} the steeper rise of F_2 is observed. This phenomena is know as *scaling violation*.

1.2.2 The Strong Coupling Constant

In QCD colored quarks (color is a new quantum number that gives the "charge"of strong forces) interact with each other via exchanging gluons which are colored too. Since states with non–zero color are observed, one assumes that colored quarks and gluons are always bounded into color neutral hadrons. This assumption is known as the *confinement hypothesis*, it implies the non-observability of free quarks: since quark carry color they are confined. On the other hand, at short distances (large Q^2) the partons behave as nearly free. The QCD Lagrangian does not contain any energy scale (neglecting quark masses), thus there is no understanding of the both regimes if the coupling constant is simply constant (a fixed number) [2, 3].

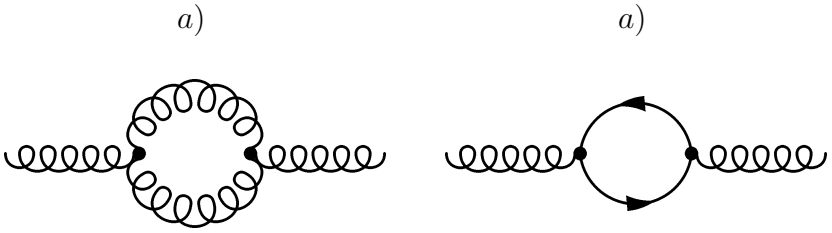

Figure 1.4: *Loops in QCD: a) gluon loop (not observed in QED) and a) fermion loop*

The non-commutativity of the $SU_c(3)$ (the symmetry group of the strong force), leads to self-interaction of the gluon field (see figure 1.4), a process which is not observed in QED. If one consider the self-energy of gluon loop (figure 1.4 *a*)) and the standard Feynman rules, a divergency appears, since one has to integrate over the momentum inside the loop up to infinity. The way to get rid of this divergence is a renormalization procedure using an arbitrary energy scale μ. The coupling constant becomes a function of Q^2which

is known as *running of the strong coupling*. The general dependence of the coupling constant in lowest order is expressed by the following relation [3]:

$$\alpha_s(Q^2) = \frac{12\pi}{(33 - n_f)\ln(Q^2/\Lambda^2_{QCD})} \tag{1.15}$$

where n_f is the number of flavors.
Since α_s decreases with increasing Q^2,

$$\lim_{Q^2\to\infty} \alpha_s(Q^2) = 0,$$

the quarks behave as free particles, a phenomenon known as *asymptotic freedom*[4].

The perturbative QCD theory is an expansion in α_s . A limit about the applicability of the expansions is the quantity Λ_{QCD}. When Q becomes comparable to $\Lambda_{QCD} \approx 200\,\text{MeV}$, α_s becomes larger than 1 and the perturbative series diverges.

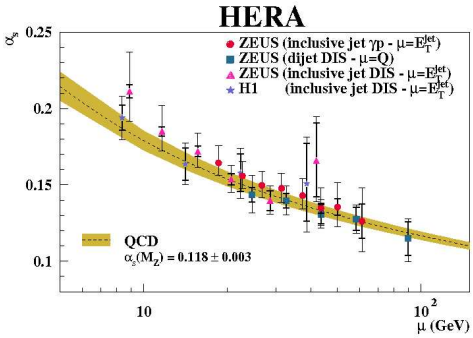

Figure 1.5: *Running α_s measured by H1 and ZEUS experiments at HERA accelerator.*

1.2.3 Parton Evolution Models

A zeroth order process (*QPM process*) means that the photon interacts directly with a quark in the proton. This scattering does not include any strong interaction. Therefore it does not depend on α_s and is interpreted as *zeroth order α_s process* (see figure 1.2).

In contrast with zeroth order, *first order* processes contain one gluon vertex. This means that the photon interacts with a $q\bar{q}$ pair created from

[4]Predicted by Politzer, Gross and Wilczek in 1973, the Nobel prize winners in 2004. This is shown by data from HERA experiments– H1 and ZEUS.

gluon splitting in the proton. This phenomenon is known as *Boson-gluon fusion* (see figure 1.6 *a*)). Another first order process is the *QCD-Compton effect* where the photon scatters of a quark that emits a gluon (see figure 1.6 *a*)). The cross sections for these processes are proportional to α_s.

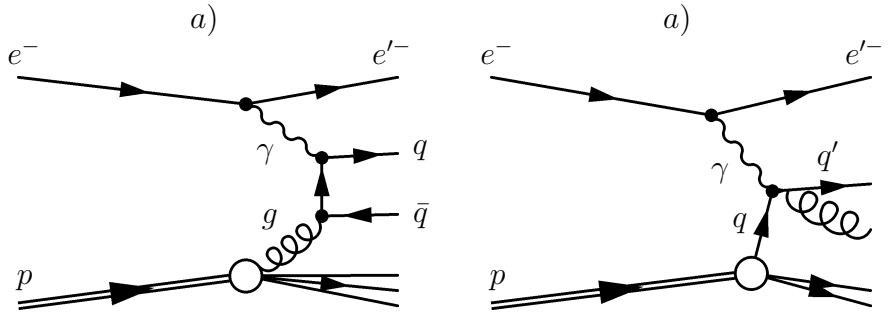

Figure 1.6: *First order α_s processes. a) Boson gluon fusion ; a) QCD Compton effect*

In contrast to QED, where the expansion is approximated with first order of α_{em}, in QCD higher order processes have to be considered. This fact can be explained by the behavior of the two couplings: $\alpha_{em} \approx 1/137$ while α_s is not so small and even becomes larger with decreasing Q^2. Thus higher order corrections can not be neglected. Analytical calculations are available up to the second power of α_s, higher order processes have to be approximated by other approaches.

Higher order processes, as shown in figure 1.7, are treated in terms of parton density functions (pdf) and the evolution equation given by few models (DGLAP, BFKL and CCFM). The DGLAP evolution equation considers all processes including gluon radiation and gluon splitting.

- **DGLAP** In the **D**okshitzer, **G**ribov, **L**ipatov **A**ltarelli and **P**arisi approach [3, 4] the parton densities depend on Q^2. The scale dependence of the parton distribution functions is originating from processes such as gluon radiation from quark $q \rightarrow gq$ or a gluon $g \rightarrow gg$ and creation of quark-antiquark pair $g \rightarrow q\bar{q}$. Not only the emission of one gluon but two or n gluons have to be considered. The dependence of the pdf on Q^2 is described by the DGLAP integro-differential equations:

$$\frac{\partial f(x,t)}{\partial t} = \frac{\alpha_s(t)}{2\pi} \int_x^1 \frac{dz}{z} \left(P_{qq}(z) f(\frac{x}{z}, t) + P_{qg}(z) g(\frac{x}{z}, t) \right) \qquad (1.16)$$

$$\frac{\partial g(x,t)}{\partial t} = \frac{\alpha_s(t)}{2\pi} \int_x^1 \frac{dz}{z} \left(P_{gq}(z) g(\frac{x}{z}, t) + P_{gg}(z) f(\frac{x}{z}, t) \right) \qquad (1.17)$$

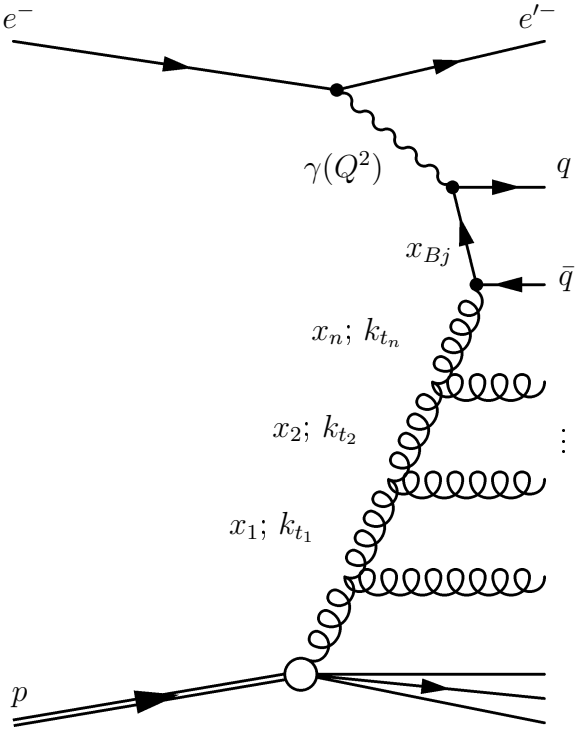

Figure 1.7: *Diagram for higher order processes.*

where $t = \ln(Q^2/\Lambda^2_{QCD})$ and the probability that a parton j with four-momentum k and longitudinal momentum fraction x_i radiates a parton with momentum $(1-z)x$ and continues with momentum zx is given by the splitting functions $P_{ij}(z)$ (see figure 1.8) [4]:

$$P_{qq}(z) = \frac{4}{3}\left[\frac{1+z^2}{1-z}\right] \tag{1.18}$$

$$P_{gq}(z) = P_{qq}(z).(1-z) = \frac{4}{3}\left[\frac{1+(1-z)^2}{z}\right] \tag{1.19}$$

$$P_{qg}(z) = \frac{1}{2}\left[z^2+(1-z)^2\right] \tag{1.20}$$

$$P_{gg}(z) = 6\left[\frac{1-z}{z} + \frac{z}{1-z} + z(1-z)\right] \tag{1.21}$$

One of the main points in the DGLAP approach is a strong ordering[5] of the virtuality. It can be written $Q^2 = k_T^2/(1-z)$, at small values of z, this leads to strong ordering in the transverse momentum squared:

[5]ordering of the successive emitted partons in the ladder, in a given kinematic quantity.

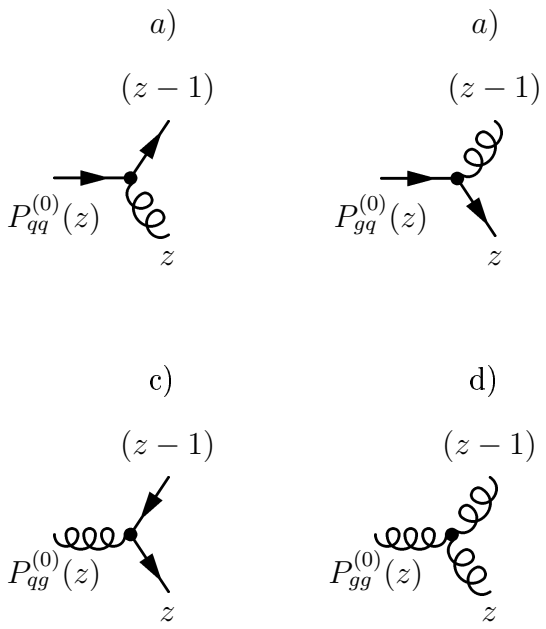

Figure 1.8: *Gluon splitting and radiation, defining the splitting functions.*

$$k_{t_0}^2 \ll k_{t_1}^2 \ll \ldots \ll k_{t_{n-1}}^2 \ll k_{t_n}^2$$

Each parton, n, carries much larger transverse momentum than the parton, $n-1$. All parton transverse momenta are limited from below by a fixed value Q_0^2, at which the evolution starts and from above, by the photon virtuality Q^2.

DGLAP provides a good description of the inclusive structure function F_2 for moderate values of x_{Bj}. At low x_{Bj}, an increase of F_2 with decreasing x_{Bj} is observed. The DGLAP description of data is not always satisfactory. Deviations from predictions are observed when differential cross sections or exclusive processes like forward jet and particle production are investigated.

DGLAP at Small x_{Bj}

At small x_{Bj} the behavior of the parton parameterization functions is dominated by the splitting functions $z \to 0$:

$$P_{qq} \to \frac{4}{3},\ P_{qg} \to \frac{1}{2},\ P_{gq} \to \frac{8}{3z},\ P_{gg} \to \frac{6}{z}$$

The gluon splitting functions are the most singular with largest coefficient. The DGLAP equation becomes dominated by the behavior of the gluon splitting functions and the equation for the gluon distribution can be written:

$$\frac{\partial g(x,Q^2)}{\partial \ln Q^2} = \int_x^1 \frac{dz}{z} P_{gg}(\frac{x}{z},\alpha_s) g(\frac{x}{z},Q^2) \tag{1.22}$$

The solution of this equation gives a steep rise of the gluon distributions.

- **BFKL** (**B**alitsky, **F**adin, **K**uraev and **L**ipatov) [4] In this calculation, the evolution of the parton distributions is performed under the requirement of strong ordering in x_i:

$$x_0 \gg x_1 \gg \ldots \gg x_{n-1} \gg x_n$$

The x_i values are limited below from the Bjoerken x_{Bj}. The evolution equation is:

$$\frac{df(x,k_t)}{d\log(\frac{1}{x})} = \int dk_t'^2 K(k_t^2,k_t'^2) f(x,k_t'^2) \tag{1.23}$$

Where k_t is the transverse momentum of the parent parton, $k_t'^2$ is the transverse momentum of its daughter and $K(k_t^2,k_t'^2)$ is the *BFKL kernel*. The function $f(x,k_t'^2)$ is related to the DGLAP gluon density $g(x,Q^2)$ by:

$$xg(x,Q^2) \simeq \int_0^{Q^2} \frac{dk_t'^2}{k_t^2} f(x,Q^2) \tag{1.24}$$

There is no requirement in the ordering of the transverse momenta. BFKL is applicable for small x_i.

- **CCFM** The **C**atani, **C**iafaloni, **F**iorani and **M**archesini [5] approach requires ordering of the gluon ladder in the quantity $q = \frac{p_t}{1-z}$ where p_t is the transverse momentum of the emitted parton and z is the fraction of the parent momentum carried by the emitted parton. Since $p_t = q^0 \cdot \sin\theta$ ordering in emission angle is required:

$$\theta_{i+1} > \theta_i$$

The CCFM approach works in both regimes, at small x_{Bj}, where BFKL is appropriate and at large x_{Bj}, where DGLAP's predictions are reliable.

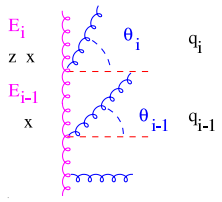

Figure 1.9: *Angular ordering in the CCFM evolution model*

The phase space for the three approaches described above is presented in figure 1.10.

1.3 Photoproduction and D^*

The regime at small or vanishing virtuality ($Q^2 \ll 1\,\mathrm{GeV}^2$) is called *Photoproduction*. In this case the mass of the virtual photon comes close to its mass shell and the photon can be considered as quasi–real.

If the photon interacts directly with a parton of the proton the process is called *direct photoproduction*. If the quasi real photon fluctuates into bounded hadronic state– vector meson– the photon is called *resolved*. When it splits up into a quark-antiquark pair the component is called *anomalous*. Photoproduction events where the photon evolves a hadronic structure are called *resolved photoproduction*.

Since the cross section (1.14) is proportional to $1/Q^4$, photoproduction dominates the total ep cross section.

1.3.1 Heavy Quark Production and Hadronisation

The dominant process for heavy quark production is *boson gluon fusion*. In contrast to light quarks, where $m_q \approx \Lambda_{QCD}$ the masses of the heavy quarks

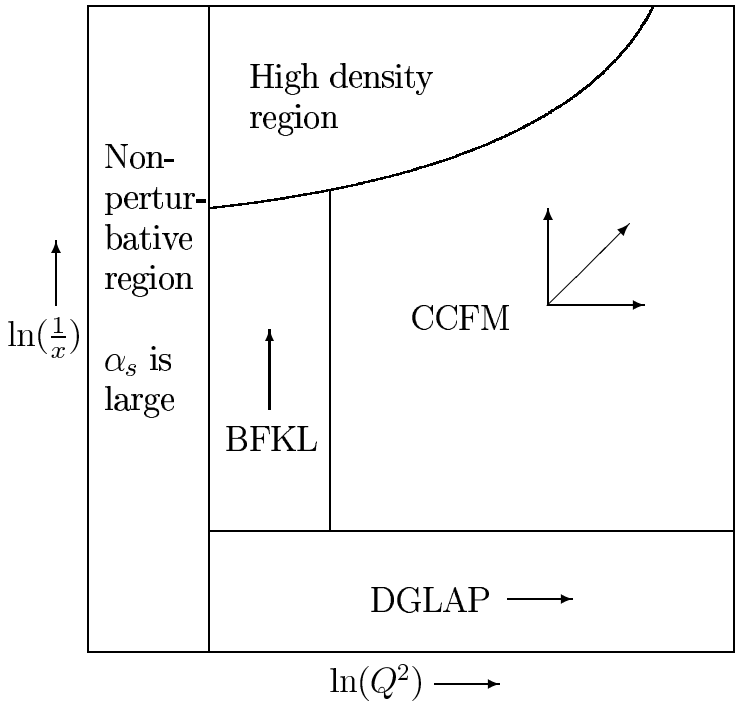

Figure 1.10: *Applicable regions of the DGLAP, BFKL and CCFM evolution approaches.*

fulfill $m_Q \gg \Lambda_{QCD}$ so they can provide a large enough scale, such that perturbative QCD predictions even at low values of Q^2 ($Q^2 \ll 1\,\mathrm{GeV}^2$) are reliable.

The lightest heavy quark in the standard model (SM) is the *charm* quark. It has a mass $m_c \approx 1.5\,\mathrm{GeV}$ and with a probability of $25.5 \pm 1.7\,\%$ it fragments into a $D^{*\pm}$ meson [6]. The D^* meson consists of a charm and a down quark and it can be considered as a sign for charm quark identification.

The process of transition between colored partons to colorless hadrons is called *hadronisation*. There are a few theoretical models that describe hadronisation. In this thesis only the *Lund String Model* is used.

- **The Lund String model** [7, 8]
  The basic idea in the Lund string model, is that the quark-antiquark pairs are bound via one-dimensional colored flux tubes called *string*. The force between the quarks increases with the distance linearly $F \propto r$. When the energy of the string is large enough to create a new quark pair, the string "breaks". On the other hand if the new pair has energy enough, it can split into another pair and so on. The process continues until the string has not enough energy to create new pairs and the

quarks combine into colorless hadrons.

1.4 Monte Carlo Event Generators

Theoretical predictions in high energy physics are usually done using *Monte Carlo (MC) event generators*. Based on Monte Carlo methods for solving integrals, they calculate the probabilities of different interactions and generate the four-vectors of the particles produced in different levels of the interaction. In this thesis two MC event generators are used. RAPGAP 3.01 [9], based on the DGLAP evolution model and CASCADE 1.20 [10, 5] based on the CCFM evolution model (both discussed in section 1.2.3).

The way MC generators describe the particle interaction can be divided into different stages. The description of the hard partonic sub-process, up to leading order of α_s, is calculated from *Matrix Elements* (ME) given by perturbative QCD calculations. Initial and final state *parton showers* (PS) are used to approximate higher order processes. The initial state parton showers are evolved from the hard interaction to the proton (backward scheme) using different evolution models. The initial partons (of the hard scattering) can branch into new partons, thereby creating the final state parton shower. The transition from partons to observable hadrons, hadronisation, occurs via strong interaction at large values of α_s and models (like the Lund-String model implemented in JETSET/PYTHIA) have to be applied.

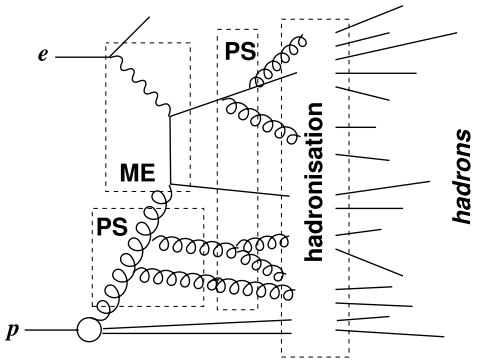

Figure 1.11: *Different stages in MC event generators: hard interaction, initial and final QCD radiation and hadronisation*

In the following the MC generators used here are briefly described:

- RAPGAP: The QCD radiation is done in terms of parton showering, based on DGLAP evolution equations. The evolution starts on the photon side and continues to the proton side, down to a cut-off value of Q_0^2. The partons of the ladder are strongly ordered in the transverse

momentum squared, $k_\perp^2$. In RAPGAP quasi–real resolved photon processes are also included. The charm quark are usually produced via BGF. The so-called *charm–excitation* also has significant contribution to charm production. In this process a charm quark from the photon side interacts with a gluon from the proton side. In the generator the concept for resolved real photons is extended for resolved virtual photons. This occurs when the virtuality of the photon is significantly smaller than the factorization scale of the hard sub–process. For the hadronisation the Lund-String model is used.

- CASCADE : In CASCADE the probability for a parton to branch is given by the CCFM evolution equation. The matrix elements depend on $k_\perp$. The evolution is developed from the hard scattering to the proton again, but requires angular ordering of the gluons. In CASCADE no resolved processes are included implicitly. The hard sub-process is BGF and the Lund-String model is used. The CCFM un-integrated gluon density used is *set A0*.

1.5 Jets and Jet Definitions

A *jet* is a flow of particles, strongly collimated in one direction. There is not a unique definition of a jet, but there are several so-called *jet algorithms*. In general they are separated in two big groups called *cone* type and *cluster* type. They have been applied for different types of interactions. In $p\bar{p}$-collision cone algorithms were used and in e^-e^+ annihilation the clustering algorithms were used.

Jet algorithms starts from individual particles, like parton, hadron, etc. called *seed* particles and combine them into possible jets, called *proto-jets* and after applying an iterative procedure the algorithms construct the final jets. The iterative procedure stops when all particles belong to proto-jets. After satisfying additional conditions, they are selected as jets. The algorithms have to be safe concerning *infrared* (emission of a low energetic gluons) and *collinear* emission. In this thesis two of them will be discussed in detail:

- **CDF-CONE Algorithm** [11] According to the CDF-CONE algorithm, a jet can be defined from the particles which belong to a cone centered around the seed particle (particles with transverse momentum above threshold $E_t > E_0$), with a radius R, defined in (η, ϕ)-space:

$$R = \sqrt{\Delta\eta^2 + \Delta\phi^2} = \sqrt{(\eta_i - \eta_0)^2 + (\phi_i - \phi_0)^2}$$

where η_i is the pseudo rapidity of the particle i and ϕ_i is the azimuthal angle. η_0 and ϕ_0 are the center of the cone after summing the transverse momenta of all particles in the cone. If the direction of the center of gravity of the summed particles do not agree with the direction of the seed particle, it becomes the seed of a new cone. The iterations continues until the directions of the center of gravity and the seed agree. This cone is then considered as a jet.

- **Inclusive k_t Algorithm** [12] The algorithm combines proto-jets, if they are close enough in (η, ϕ)-space, the distances are defined with their transverse momenta p_t. The idea is that proto-jets which are close are joined and form new proto-jet.

  The inclusive k_t algorithm can de applied in the following steps:

  1. For each proto-jet i define:

     $$d_i = p_\perp^2$$

     and for each pairs of proto-jets :

     $$d_{ij} = min(E_{\perp,i}^2, E_{\perp,j}^2)\frac{(\eta_i - \eta_j)^2 + (\phi_i - \phi_j)^2}{R_0^2}$$

     with R_0 being a parameter of the algorithm which is of the order of 1.

  2. Find the smallest of all the d_i and d_{ij} and label it with d_{min}

  3. If d_{min} is d_{ij}, then cluster proto-jets i and j are clustered into new proto-jet k, with the kinematic quantities:

     $$\begin{aligned} p_{\perp,k} &= p_{\perp,i} + p_{\perp,j} \\ \eta_k &= \frac{p_{\perp,i} \cdot \eta_i + p_{\perp,j} \cdot \eta_j}{p_{\perp,k}} \\ \phi_k &= \frac{p_{\perp,i} \cdot \phi_i + p_{\perp,j} \cdot \phi_j}{p_{\perp,k}} \end{aligned}$$

  4. If d_{min} is d_i, then the proto-jet i is removed from the list of proto-jets and is considered as jet.

  5. The procedure continues until there are no proto-jets left in the list.

The observation of free quarks and gluons in nature is not possible since they cary color. They can exist only in colorless states combined with other partons– the mesons and baryons. The decay of the hadrons produces jets. It is expected that the jets are well correlated in momentum and angle with the parton that produced them. For that reason it is very important to study jet production.

Chapter 2

HERA and the H1 Experiment

In this chapter a brief description of the HERA accelerator and the main components of the H1 detector is presented.

2.1 The Hadron Electron Ring Accelerator (HERA)

The HERA ring accelerator is located at the DESY laboratory, Hamburg, Germany. It accelerates electrons and protons to energies 27.6 GeV and 920 GeV respectively. Bunches of the particles collide every 96 ns at tow interaction points where ZEUS and H1 detectors are located. They were build to detect the products of this high energetic ep collisions.

2.2 The H1 Experiment

The H1 detector is a complex device, designed to measure the momentum and energies of high energetic particles and jets produced in the collision. It consist of many sub-detectors, with different purposes[1].

Due to the larger energy of the protons, the particles produced from the collision are expected to be emitted mainly in forward direction (the direction where z is positive). Therefore the detector was build asymmetrically. A general view of the detector and its sub-detectors is given in figure 2.1.

[1]In the H1 coordinate system, the z-axis is collinear to the proton direction, y is perpendicular to the ground and the x-axis is oriented to the center of HERA. The azimuthal angle ϕ is measured in xy plane, and the polar angle θ is measured from z axis, $\theta = 0^\circ$ in the proton direction and $\theta = 180^\circ$ in the electron direction.

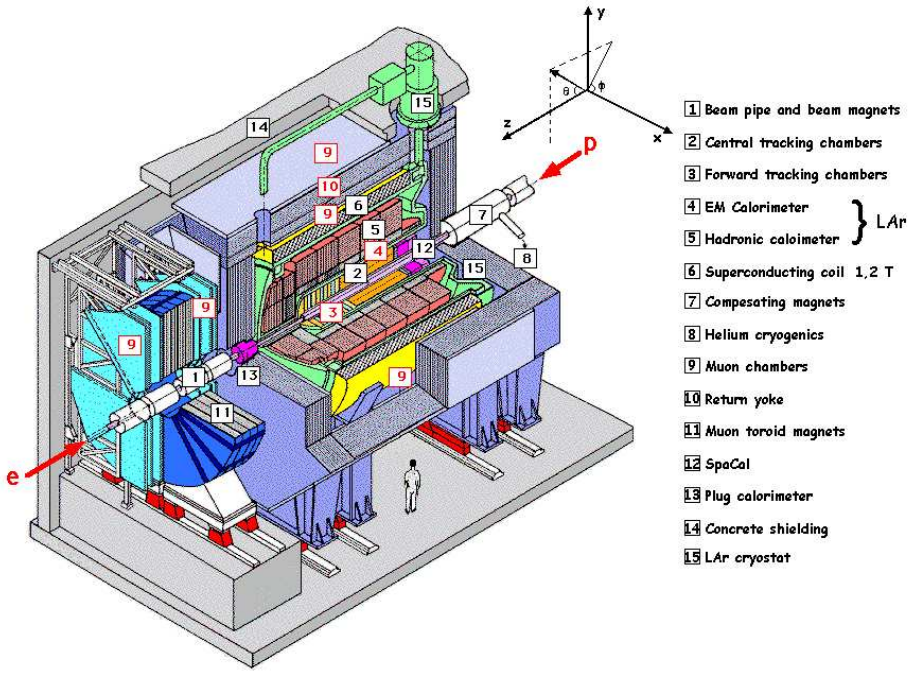

Figure 2.1: *The H1 detector for HERA*

The interaction point is surrounded by the central (2) and forward (3) tracking chambers which are inside the Liquid Argon (LAr) calorimeter- (4) electromagnetic and (5) hadronic sections. The SpaCal (12), situated outside the beam pipe in the backward region, has electromagnetic and hadronic parts. With them, almost the whole solid angle is covered. A cylindric superconducting coil (6), covering the calorimetry and tracking chambers, produces a magnetic field of strength $1.2\ T$. The magnetic field is parallel to the beam pipe. The detector is covered by the return yoke (10), introduced also to detect muons and the energy leaking trough the other sub-detectors.

In the following sections, a short description of the tracking, calorimetry and triggering system of the detector is given.

2.2.1 Tracking

The tracking system covers a range in pseudo rapidity $-3 < \eta < 2.8$ and consists of the following components:

- **Silicon tracker**: central and backward silicon tracker (CST and BST), measures the hits of charged particles via ionization in semiconductors. They cover the polar angle $30° < \theta < 150°$ and $162° < \theta < 176°$

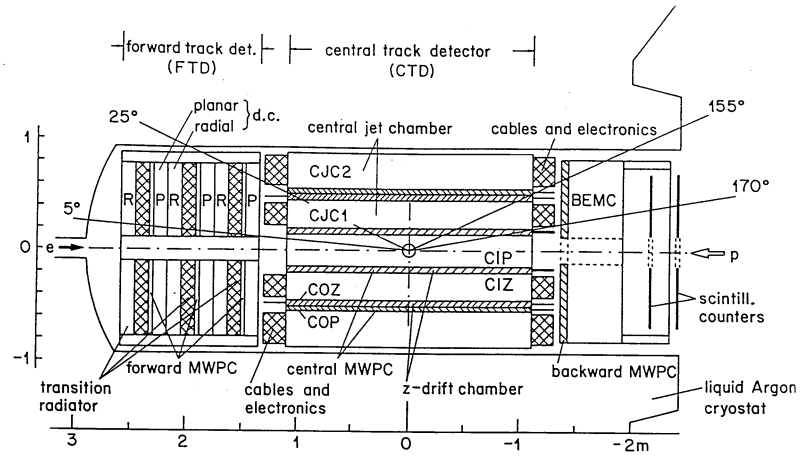

Figure 2.2: *The central and forward tracking system of H1*

respectively. Located very close to the interaction point, they have very high resolution.

- **Central detectors**: Outside the silicon trackers, the central tracking detector consist of six chambers. It consist of the Central Inner Proportional Chamber (CIP) and the Central Inner z Chamber (CIZ). They are followed by the Central Jet Chamber (CJC1), the Central Outer z Chamber (COZ), Central outer Proportional Chamber (COP) and the outer Central Jet Chamber (CJC2). The CJC1 and CJC2 measures the direction and momentum of the particles via ionization in a gas. Together they cover a polar angular range of $15° < \theta < 165°$. The momentum resolution for charged particles is $\sigma_p/p^2 < 3 \times 10^{-3}\,\mathrm{GeV}^{-1}$ (p is the particle momentum) and the angular resolution is $\sigma_\theta \approx 1\ mrad$.

- **Forward Tracking** The Forward Tracking Detector (FTD) covers a polar angle of $5° < \theta < 30°$ and consists of three so-called super modules each of them including forward proportional chamber, radial and planar drift chambers and transition radiator as shown in figure 2.2.

A schematic view of the tracking system is shown in the figure 2.2.

2.2.2 Calorimeters

The main task of the calorimeters of H1 is to identify neutral and charge particles, measure their energy and to detect jets in the form of energy clusters. It surrounds the tracking system and contains lead (iron) plates with active

material Liquid argon (LAr) for the electromagnetic (hadronic) part. It is a sandwich type calorimeters and consist of an inner electromagnetic (EM) and an outer hadronic (HAD) part. The EM part covers the polar angular range $4° < \theta < 153°$. To identify the hadrons in the very forward region, the Plug calorimeter is used. It covers the polar angle of $0.6° < \theta < 4°$. The SpaCal has also an EM part and HAD section. It is mainly used to detect the scattered electrons. It covers the angular range of $153° < \theta < 177.5°$, i.e. $1 < Q^2 < 100\,\mathrm{GeV}^2$. In terms of pseudo rapidity the LAr and the SpaCal cover the regions of $-3.8 < \eta < 3.6$.

Other important units that make H1 a general purpose detector for all kind of elementary particles are:

- **Muon System**: Designed to detect muons, the muon system consists of two subdetectors, central and forward. The forward muon spectrometer covers a polar angular range of $3° < \theta < 17°$ and has a good resolution for large muon momenta.

- **Time-of-flight system**: The Time-of-flight system is located at both ends of the detector along the beam pipe. It is made of scintillators with a good time resolution of $1ns$ and has the purpose to reject background, related to beam-gas and beam-wall interactions.

- **Luminosity system**: The luminosity measurement is done via the Bethe-Heitler process, $ep \longrightarrow ep\gamma$, for which the cross section is very well known, the detection of this process allows to calculate the luminosity.

- **Trigger System**: At HERA electron and proton bunches crosses each 96 ns corresponding to a frequency 10.4 MHz. Only around 10 kHz is the rate of ep reactions. The background processes are several orders of magnitude higher than the interesting ep collisions. This short time between two bunch crossing will make the dead time of the detector extremely high. The rate for real DIS type events is of the order of 10 Hz. For these reasons a stable and efficient trigger system is needed.

  The H1 trigger system consist of the following trigger levels:

  - **L1**: The detector information for every bunch crossing is stored in a buffer (the so–called pipeline). The length of the pipeline corresponds to 25 bunch crossings and this is the time limit for a level 1 (L1) decision. If the decision is *keep* the pipeline is stopped. This decision is based on trigger signals from different detector components– *trigger elements* (TE). The total number of

TE are logically combined into 128 subtriggers (ST). If one of the ST accepts an event the decision of L1 is positive. L1 reduces the rate from 100 kHz to 1 kHz. When the pipeline is stopped the detectors is not able to record new events (dead time starts).

- **L2**: If the event is accepted by the first level it passes to the second level L2. It has 20 μs time to make the decision. If the decision is reject, the L1 pipelines are cleared and information from the detector can be stored. If the decision is positive the detector is read out. L2 reduces the rate from 1 kHz to 50 Hz.

  A third level L3 was not implemented for the data analyzed here.

- **L4**: At L4 a computer farm is used for full event reconstruction. The forth level does not contribute to the dead time.

More information about the detector can be found in the detailed description in [13] and [14].

Chapter 3

Photoproduction of D* mesons

In this chapter a Monte Carlo (MC) study of a D^* meson and D^* mesons associated with a jet in photoproduction is presented. For this purpose the RAPGAP (only direct photons were considered) and the CASCADE MC event generators were used.

Events containing charm quarks in the direct photoproduction regime and a charm jet are investigated. The charm is tagged via a D^* meson. The jet that contains the D^* is called D^*-jet and the others simply jets. If an event contains two D^* mesons, they are considered like two separated events with a D^*.

The identification of the charm jet is done from a pure geometrical point of view. A distance between the D^* and the jet is defined in $\eta - \phi$ space with the variable $R = \sqrt{\Delta\eta^2 + \Delta\phi^2}$ where $\Delta\eta = \eta^{D^*} - \eta^{jet}$ and respectively for $\Delta\phi$. Then the charm jet is the one with minimal R.

The photoproduction regime is selected with cuts on the virtuality: $Q^2 < 0.01\,\mathrm{GeV}^2$ and the inelasticity $0.29 < y < 0.65$ which is related to the energy of the photon. The D^* and the jets are required to have: $p_t > 2.0\,\mathrm{GeV}, |\eta| < 1.5$. With these cuts the events are expected to be in the central region of the H1 detector. A summary of the cuts is given in table 3.1

The jets are identified using **Inclusive** k_t algorithm (discussed in section 1.5).

Differential Cross Sections

In figure 3.1 the differential cross sections as a function of the transverse momentum $d\sigma/dp_t$ of D^* and D^*-jet are shown as obtained for RAPGAP and CASCADE. In general the shapes of both generators are similar but the cross section from CASCADE is larger especially for large p_t. In CASCADE , applying the CCFM scheme, there is no ordering in the transverse momenta

Q^2	$Q^2 < 0.01\,\mathrm{GeV}^2$
y	$0.29 < y < 0.65$
$p_t(D^*\&jets)$	$p_t > 2.0\,\mathrm{GeV}$
$\theta^\circ(D^*\&jets)$	$25^\circ < \theta^\circ < 155^\circ$

	RAPGAP	CASCADE
total cross section	160.2 $[nb]$	458.6 $[nb]$
the cross section after the selection	3.6 $[nb]$	4.6 $[nb]$

Table 3.1: *Summary of the applied cuts*

of the gluons in the ladder, but only in the emission angle. It can happen that a gluon has higher p_t than the quark, which is forbidden in RAPGAP (because of p_t ordering). The correlation between the momenta of the D^* meson and the D^*-jet are shown in figure 3.2. In general the p_t of the D^* jet is higher than the p_t of the D^*. The D^* carries around 70% of the jet momentum.

The angular distribution of D^* meson and D^*-jet are shown in figure 3.3. The D^* is found mainly in the electron direction, since it follows the direction of the photon.

The distribution of the transverse momenta and the rapidity of jets **not** containing the D^* are shown in figure 3.4.The distributions look different from the D^*–jet results. The jets without the D^* meson show a softer p_t spectrum than the D^*–jets and the η distribution is flat while that for the D^* jets have a maximum at negative η which corresponds to the region toward the photon direction. Differences appear between RAPGAP and CASCADE for positive regions of η. There is a slight tendency, that the CASCADE predictions for the cross section are larger for positive values of η than RAPGAP. The positive η defines a region away from the photon (closer to the proton direction) where initial radiation should indicate differences between the models. However, the η range is not large enough to draw stronger conclusions.

If one considers events with a D^* and a jet, information for further gluon radiation can be extracted. In the center-of-mass system, if there are two partons the process is back-to-back, due to momentum conservation. In photoproduction, the longitudinal Lorentz boost along the z axis, does not change the topology in the xy plane, therefore in the laboratory frame the partons have to be back-to-back. In such case, the difference between the azimuthal angles of the D^* and the jet have to be $\Delta\phi = \phi(D^*) - \phi(jet) = 180^\circ$ and they have to be balanced in transverse momentum, $\mathbf{p}_t^{D^*} = -\mathbf{p}_t^{jet}$.

However, higher order processes, hadronisation and etc., can break this balance and lead to small $\Delta\phi$ values. This effect can be seen in the $\Delta\phi$ distribution shown in figure 3.5. Both, RAPGAP and CASCADE do not exhibit

significant differences. The initial QCD radiation is responsible for higher order processes causes the tails of the distributions to low $\Delta\phi$. In a later chapter the same distribution is presented for an extended rapidity range for the additional jet. Significant differences are found between the models under consideration (see section 5.2 and figure 5.16).

In this chapter a correlation between the D^* meson and the D^*-jet quantities was presented. A good agreement between p_t and η spectra of the jet and the D^* meson was found. In addition to the D^*–jet, a second jet was considered in the visible range. Distributions for this second jet were presented. Good agreement between the MC models RAPGAP–direct and CASCADE is found. The distribution of difference in azimuthal angles of the D^*–other jet pair reveals that higher order processes are important. Thus it makes sense to open the phase space for the jets and to extend the rapidity region, in order to become sensitive to differences in model predictions.

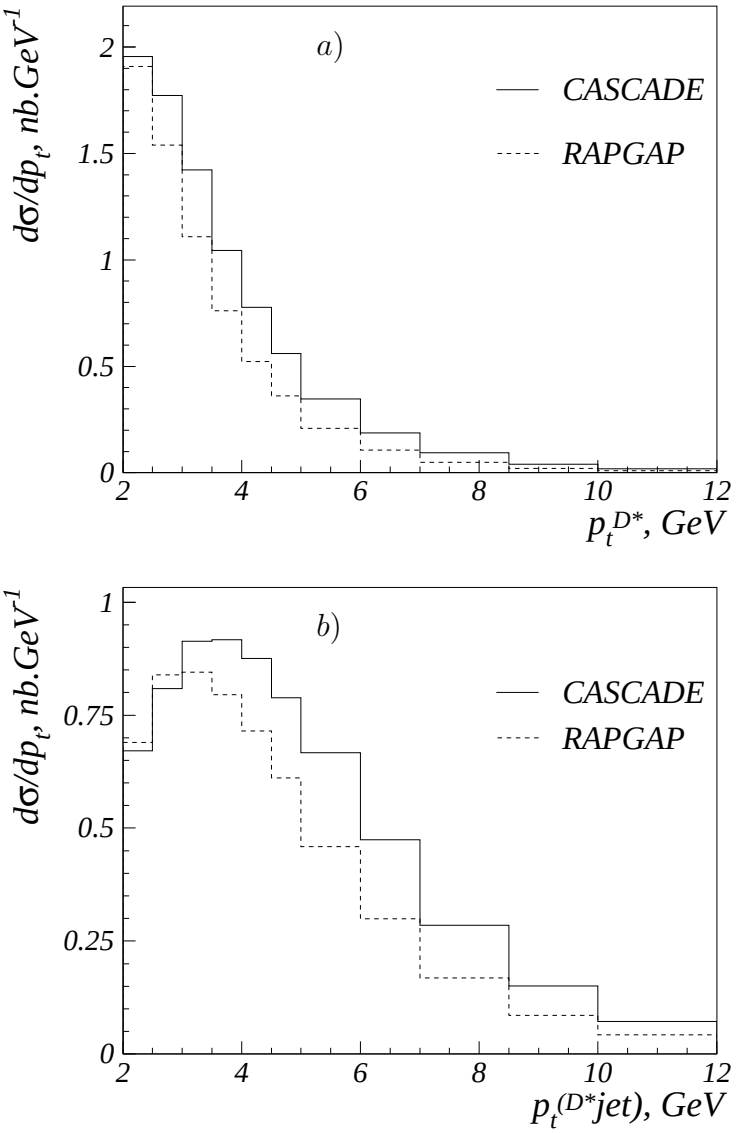

Figure 3.1: *Differential cross section $d\sigma/dp_t$ of a) $D^*$and b) D^*-jet. Shown are predictions from* CASCADE *(solid line) and from* RAPGAP *(dashed line).*

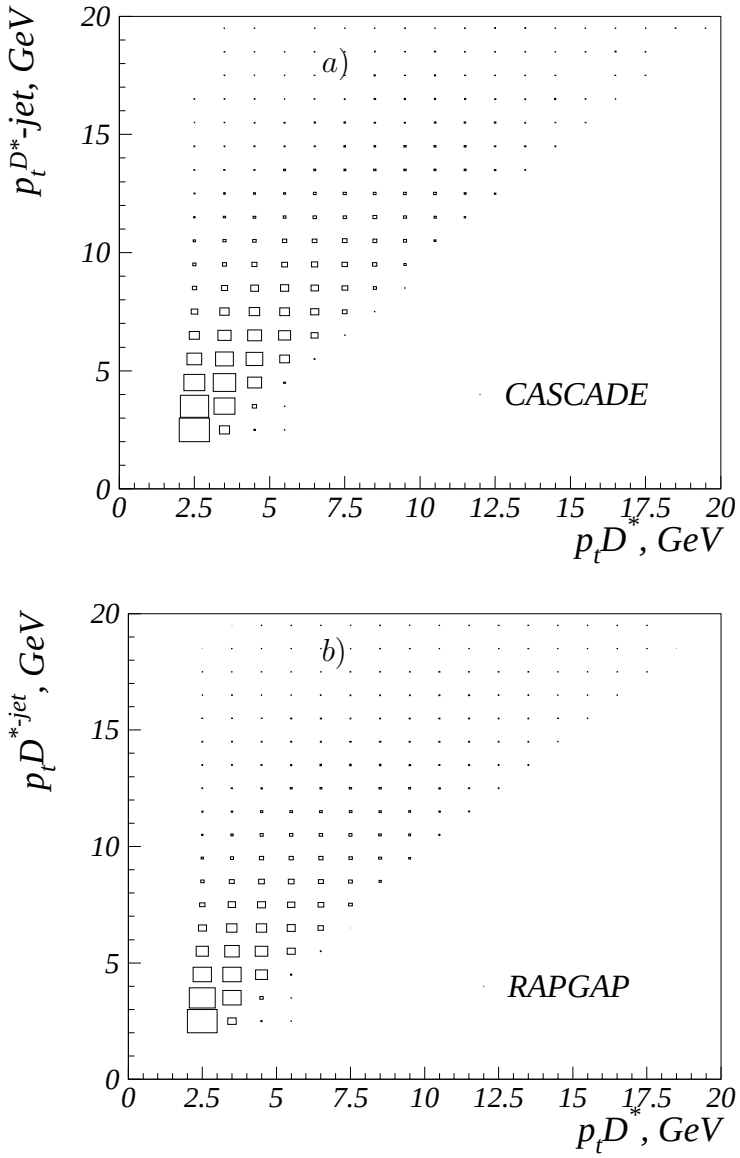

Figure 3.2: *Correlation of the transverse momenta of* D^* *(on the* x *axis) and* D^**-jet (on the* y *axis)* a) RAPGAP *and* a) CASCADE .

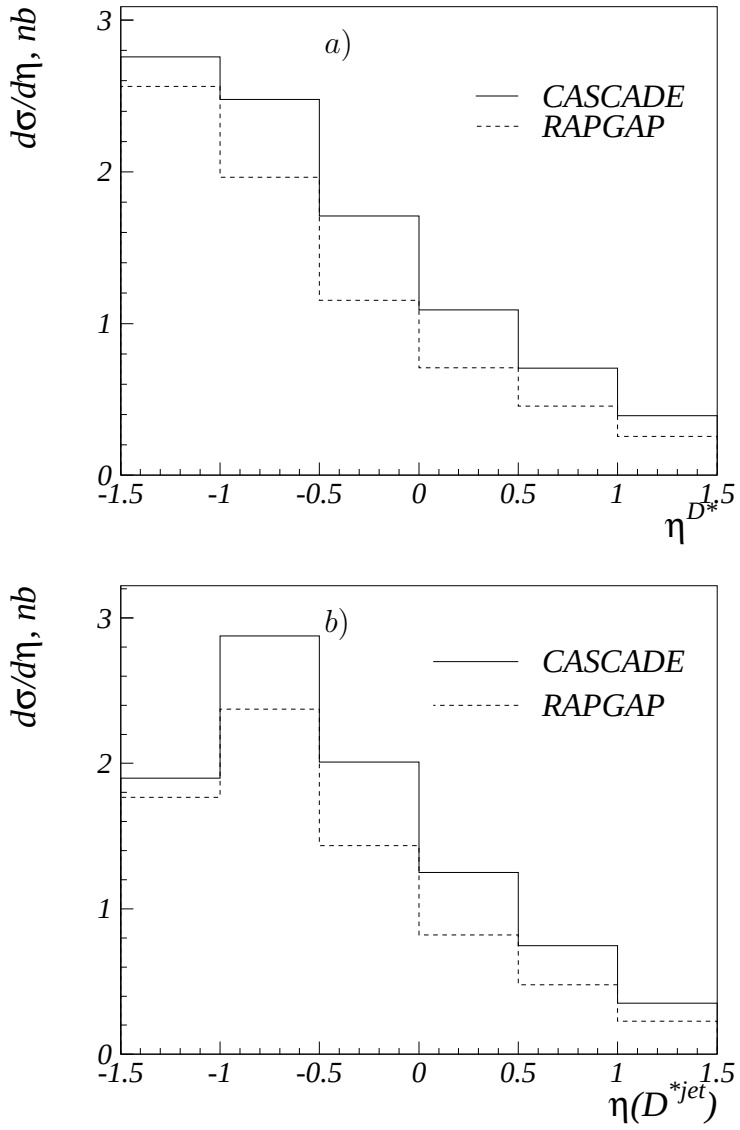

Figure 3.3: *Differential cross section $d\sigma/d\eta$ of a) $D^*$and b) D^*-jet.*

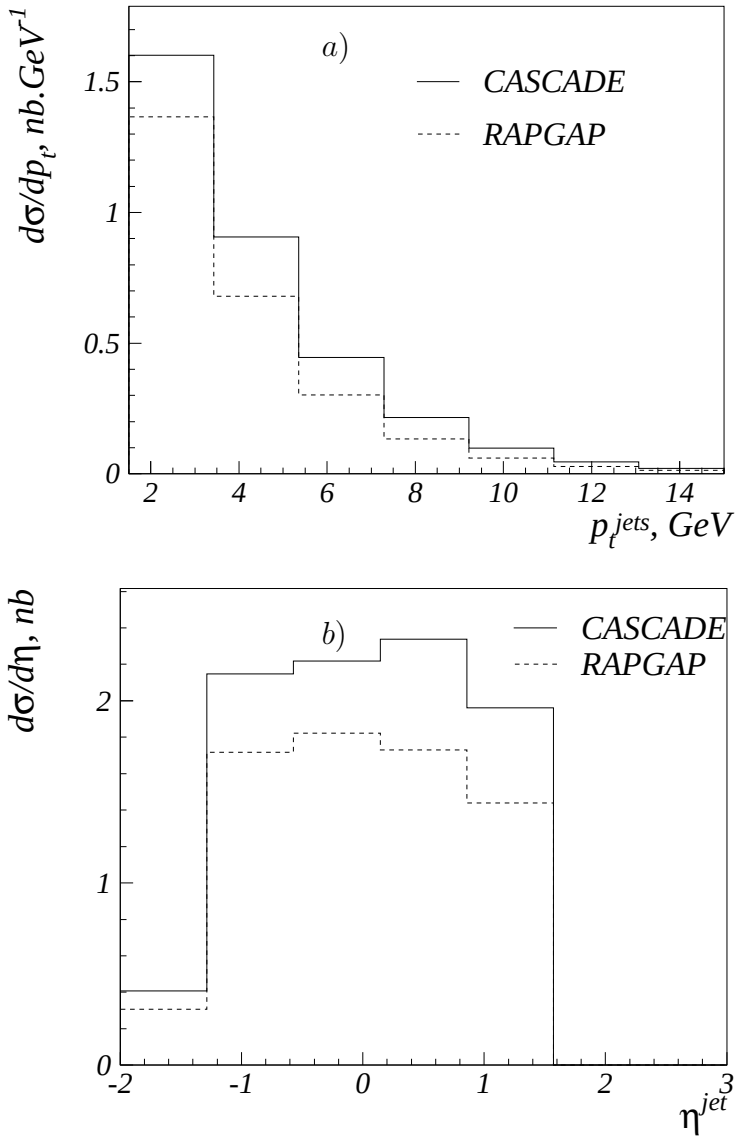

Figure 3.4: *Differential cross section in bins of a)* p_t*; and b)* η *of the jets without* D^*

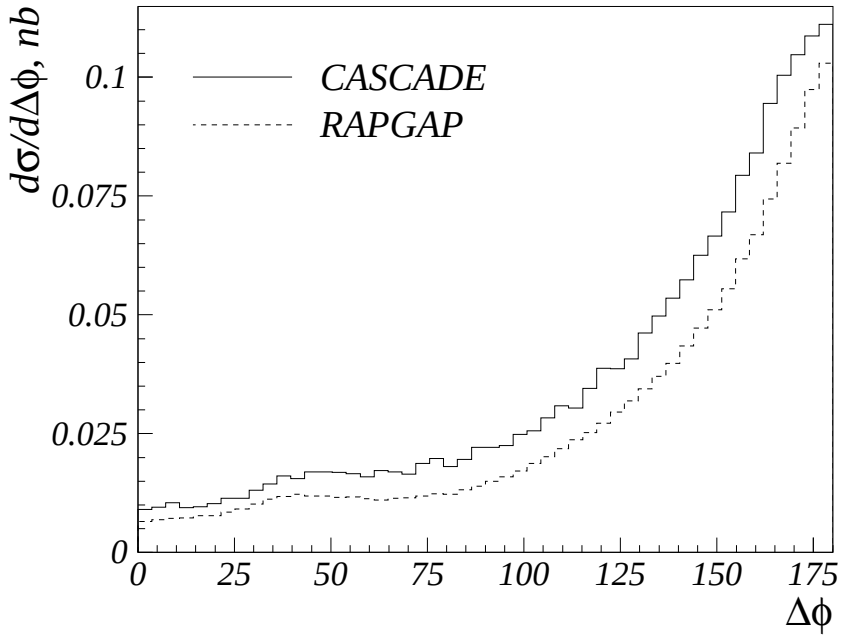

Figure 3.5: *The differential cross section $d\sigma/d\Delta\phi$. The solid line–* RAPGAP *, dashed line–* CASCADE

Chapter 4

Jets in the Forward Direction in DIS

The structure function F_2 is measured as a function of Q^2 and the scaling variable x_{Bj}. At relatively high values of x_{Bj} the behavior of F_2 is well described by the DGLAP evolution approach. But for small values of x_{Bj} and moderate or small values of Q^2 this approach is expected to fail. Since the structure function F_2 gives information about inclusive quantities, no further information for the evolution ladder can be extracted from it. Therefore exclusive processes have to be considered to extract further information.

The perturbative calculations can be done in phase space regions where α_s is much smaller than one. The running of the strong coupling depends on a scale which can be chosen to be Q^2, p_t or masses of the quarks etc. By requiring a high p_t object, e.g parton, which was radiated early in the evolution ladder, and at the same time high Q^2 in the quark box one can apply perturbative calculations at both sides of the evolution ladder. If in addition a large longitudinal momentum fraction x_i of the radiated parton is required and at the same time small x_{Bj}, there is enough phase space for evolution in x (see figure 4.1).

The relation between rapidity y and the longitudinal momentum fraction of a parton x can be written as $y \approx \ln(x)$. Considering this relation, large rapidity means large x. Therefore one assumes that a parton with large x could be found at large rapidity– close to the direction of the proton.

Since the partons are confined one is not able to observe them individually, they hadronise into jets which are observable objects. Considering the relations given above a high energetic jet found close to the direction of the proton remnant is called *forward jet*.

To study new effects at small x_{Bj}, the contributions from known results, as those coming from the DGLAP evolution, have to be considered. Thus

to suppress the DGLAP-like evolution and to open a window for BFKL-like events the following selection criteria were applied. First the squared transverse momentum of the jet is required to be of the same order as the virtuality of the photon $p_t^2 \approx Q^2$. The DGLAP evolution is performed in terms of virtualities and the hardest one is the one of the photon at the hard scattering process. This has the consequence that the probability of having partons with high transverse momentum between the proton and the hard interaction decreases rapidly (see figure 4.1). In addition the longitudinal momentum fraction of the jet defined as $x_{jet} = E_{jet}/E_p$ is required to be as large as possible in addition to small x_{Bj} at the photon side. This requirement ensures strong ordering in x_i. This idea was given by Mueller [15] thereby these jets are called *Mueller jets.*

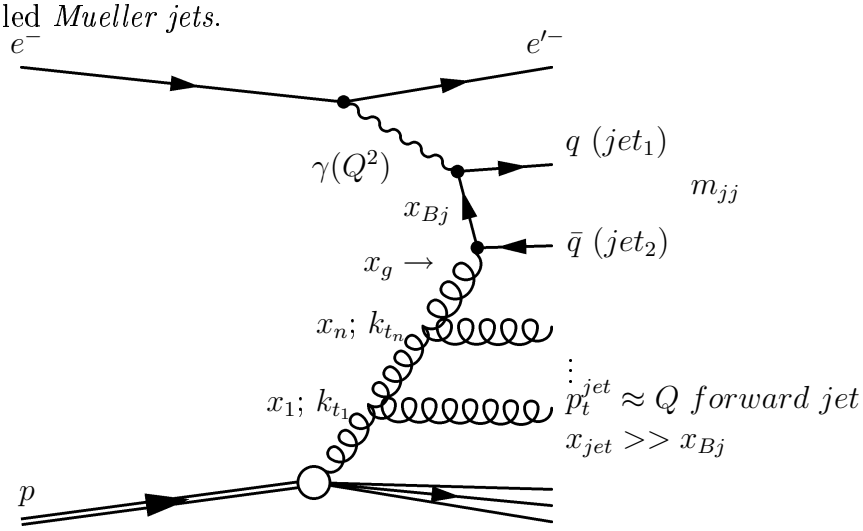

Figure 4.1: *Diagrams of parton emission*

4.1 Previous Measurements

Studying forward jets is a way to estimate the parton dynamics in a region of the phase space where x_{Bj} is rather small. In this section a brief description of the previous measurements of forward jet production with the H1 detector ([16, 17]) is presented.

The experimental data for the first analysis [16] were collected with the H1 detector during the 1994 run period. At this time HERA was colliding 27.6 GeV electrons with 820 GeV protons. The integrated luminosity of the data is 2.8 pb^{-1}.

The general selection of the data was done via the scattered electron. It was required to have an energy of at least $E'_e > 11$ GeV within the region of

polar angle $160° < \theta_e < 173°$. The kinematic variables were defined from the scattered electron: $Q^2 = 4E_eE'_e\cos^2(\theta_e/2)$ and $y = 1 - (E_e/E'_e)\sin^2(\theta_e/2)$. The scaling variable x_{Bj} was then calculated from $x_{Bj} = Q^2/(y \cdot s)$ (see equation 1.7).

The jets were defined with the CDF-cone algorithm (see section 1.4) and were accepted if they have transverse momentum of at least $p_t^{jet} > 3.5\,\mathrm{GeV}$. In order to select those jets which have transverse momentum at the same order as Q^2 only jets satisfying the following cut $0.5 < p_t^2(forward\,jet)/Q^2 < 2$ were accepted. The general cuts for the jets as well as those for the scattered electron are shown in table 4.1.

$E_{e'}$	$E_{e'} > 11\,\mathrm{GeV}$
Q^2	$Q^2 > 3.0\,\mathrm{GeV}^2$
y	$y > 1.$
x_{Bj}	$0.0001 < x < 0.004$
p_t^{jets}	$p_t^{jets} > 3.5\,\mathrm{GeV}$
E^{jets}	$E^{jets} > 28.7\,\mathrm{GeV}$
θ^{jets}	$7° < \theta^{jets} < 20°$
$0.5 < p_t^{2,jets}/Q^2 < 2$	

Table 4.1: *The general DIS cuts and the cuts for the forward jets*

The measurement as well as theoretical predictions are shown in figure 4.2. The data rise steeply towards small values of x_{Bj}. In the smallest bin the rise is hidden due to kinematic constraints. The data rise faster than the predictions based on leading order (LO+PS) DGLAP dynamics (LEPTO). The LO BFKL is clearly above the data. The data are described by calculations including contributions from resolved virtual photons RAPGAP although the model is based on k_t ordering of the partons.

In the electron-proton scattering the exchanged photon plays an important role. It may happen that the photons split into quark-antiquark pairs. These photons are called resolved. The probability for resolving the photon strongly depends on its virtuality Q^2: the smaller the virtuality the higher is the probability for resolved photons. It can be considered that in DIS where the squared momentum transfer is large, the photons become point-like and the probability for resolving photons vanishes. But if the factorization scale μ^2 is larger than the virtuality of the photon Q^2, resolved photons can give a significant contribution to the DIS cross section. In the case of the forward jets the resolved photons enlarge the cross section. It may happen that the quark connecting the photon and the gluon radiates another gluon. Thus the

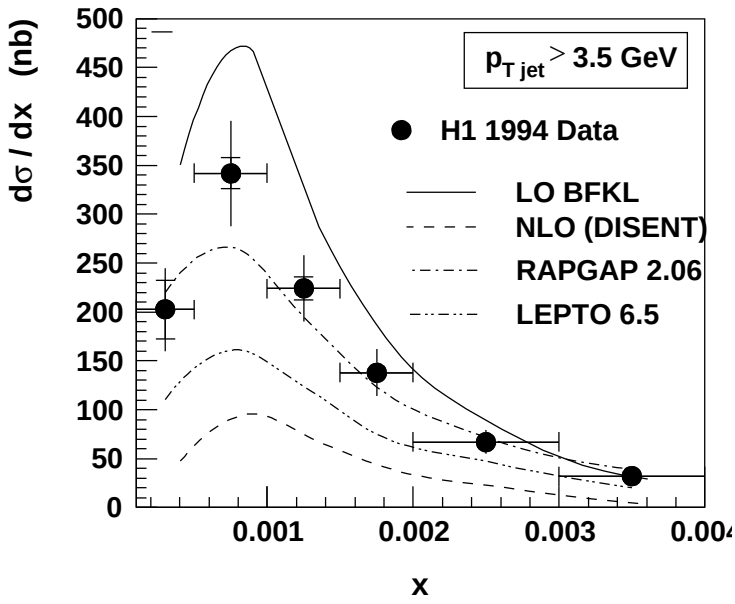

Figure 4.2: *The differential cross section for forward jets as a function of x_{Bj} as measured by the H1 collaboration for jets with $p_t > 3.5\,\mathrm{GeV}$ compared with different predictions: full line the BFKL calculations, with dashed line the NLO DISENT calculations, dash-dotted line the* RAPGAP *and dash-two dots the results form LEPTO are shown.*

DGLAP approach can be applied for the photon as well. When having the evolution ladder possible from both sides of the hard sub-process the p_t ordering starts at shifted values of η toward larger η (see figure 4.3). Thus the probability for having a high p_t jet in the direction of the proton increases. A detailed analysis of the contribution of resolved photons to forward jet cross section can be found in [18].

The forward jet analysis that has been repeated by H1 using data collected in 1997 [17] is similar to the previous one except some advantages which are briefly described. The analyzed data in this measurements correspond to an integrated luminosity of $\mathcal{L} = 13.7\ pb^{-1}$ which is roughly five times more than the data sample used in the previous measurement. This leads to smaller statistical errors in the measurement. The p_t^2/Q^2– cut was extended to $0.5 < p_t^2/Q^2 < 5$ due to resolution improvement. For better correlation of the *hadron level* and the *parton level*[1] the jet algorithm was changed to the

[1]The way to connect the measured data and the theoretical calculations is using a full set of generated colorless particles (*hadron level*) and compare it with measured tracks and clusters in the detector– (*detector level*) and the colored partons before the hadronisation (*parton level*).

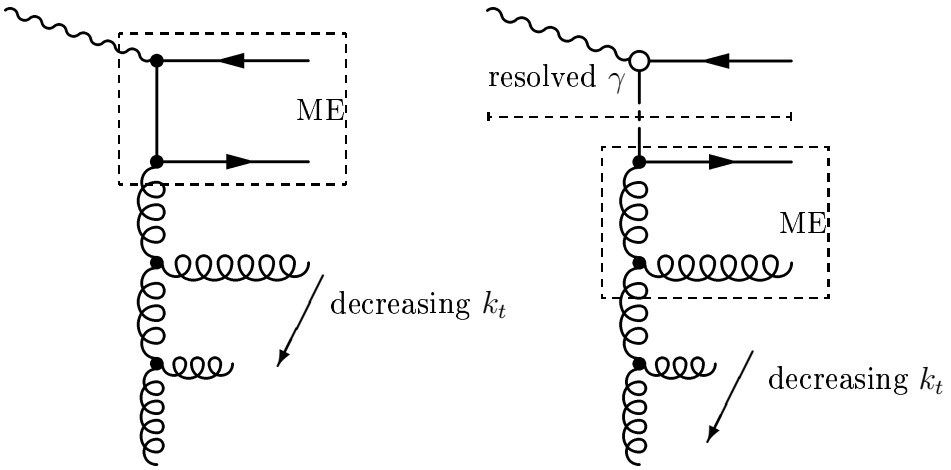

Figure 4.3: *A schematic picture for unordered parton radiation in the DGLAP approach. The left one presents the parton level BGF with additional gluons for direct photon. The right one shows the contribution of resolved virtual photons.*

inclusive k_t algorithm. Good agreement between the two analyses is found.

A New measurement [17] was performed, where in addition to the forward jet two more hard jets were required. All the three jets were required to have transverse momentum larger than 6 GeV. By requiring the same p_t-cut the p_t–ordering of the partons is disfavored. The cuts for the forward jets were kept the same (as in table 4.1) but no p_t^2/Q^2 cut was applied. The two additional jets were ordered in rapidity between the forward jet and the scattered electron $\eta_e < \eta_{jet1} < \eta_{jet2} < \eta_{fwd}$ (see figure 4.1).

Having two more hard jets one can assume that they both originate from the quark box. If the rapidity difference between the di-jet system $\Delta\eta_1 = \eta_{jet_1} - \eta_{jet_2}$ is small and rapidity difference between the forward jet and the other jet_2, $\Delta\eta_2 = \eta_{fwdjet} - \eta_{jet_2}$ is large (see figure 4.4), the probability of having evolution in x_i is increased. This scenario leads to small mass of the quark pair and thus small values of x_g are expected. Small values of x_g means that the gluon participating in the hard interaction has small longitudinal momentum fraction and leaves enough momentum for additional radiation.

On the other hand if one considers small rapidity differences between the forward jet and the di-jet system, it is very likely that one or two of the jets originate from gluons radiated close to the direction of the forward jet. If at the same time large difference $\Delta\eta_1$ is observed the phase space is larger for BFKL like evolution between the di-jet system and even between the two jets.

The cross sections as function of the rapidity differences of the three–jets

composition is shown in figure 4.5. The data are compared with a three jet next-to-leading order calculation (NLOJET++). The prediction gives a good agreement in the region where $\Delta\eta_2$ is large. If the additional jets are observed in the forward direction ($\Delta\eta_2$ gets smaller) the data are less well described. This is understood if the di-jet system originates from gluons close to the forward jet. This scenario is not included in the next–to–leading (NLO) calculation.

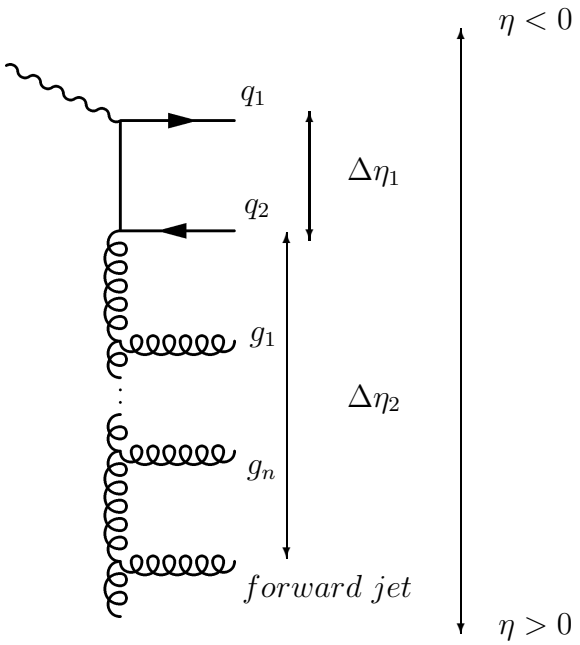

Figure 4.4: *A schematic picture of an event containing a forward jet and two more additional hard jets.*

4.2 Forward Jets with Charm quarks

Forward jets in the low x_{Bj} region can originate also from quarks via QCD–Compton-like evolution (see figure 4.6). At HERA the charm quarks are mainly produced in BGF. Thereby if one requires a charm tagged in an event which contains a forward jet then with a high probability the hard sub-process is BGF. This means that the forward jet is more likely to be induced by a gluon from the evolution ladder.

The ratio of the forward jet cross section with a tagged charm quark in the event to the cross section including all flavors is given by:

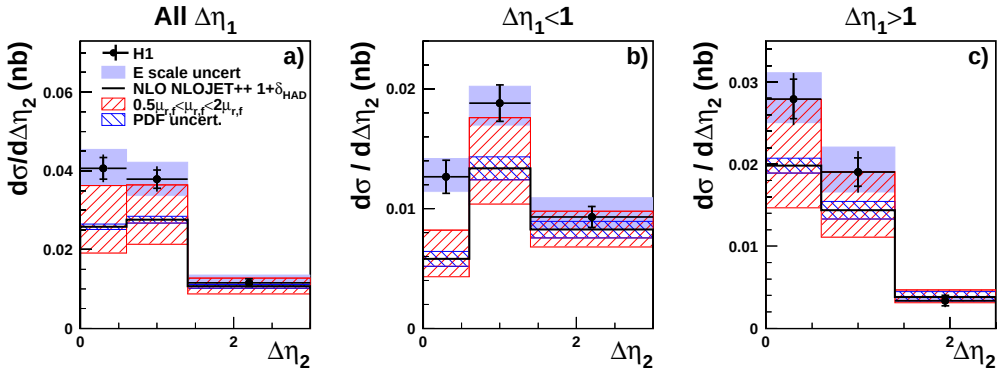

Figure 4.5: *The cross section for forward jets and two high transverse momentum jets as function of rapidity difference between the forward jet and the most forward going additional jet in intervals rapidity of difference between the two additional jets. The data is compared to NLO calculations–NLOJET++.*

$$R = \frac{d\sigma(charmquark)/dx_{Bj}}{d\sigma(all\ flavors)/dx_{Bj}}$$

This ratio R as a function of x_{Bj} is shown in figure 4.7. If one considers the sum over the charges of all active flavors the ratio is expected to be around 0.4 if the active flavors are four.

$$R = \frac{e_c^2}{\sum(e_q^2)} = \frac{4}{10}$$

Both components of the RAPGAP calculation (direct and resolved) agree with this assumption. CASCADE differs from this simple assumption. It predicts $R \approx 0.2$. Only if the charm mass is neglected the ratio $R \approx 0.4$ is recovered. This can be understood from the fact that in CASCADE only gluons are considered in the evolution ladder. Therefore the forward jet is gluon induced in contrast with RAPGAP where all possible splitting functions and partons are taken into account. But in fact the light quark induced forward jets have large contributions to the cross section which leads to the observed difference between both generators.

Investigations of the forward jet flavor shows that only $12 - 13\%$ of the forward jets originate from charm quarks for both of the MC models under consideration[2].

The perturbative calculations are done in expansions of α_s, where the strong coupling is a function of the squared momentum transfer. If Q^2 is small

[2]Please note that the investigation is on flavor of the forward jet.

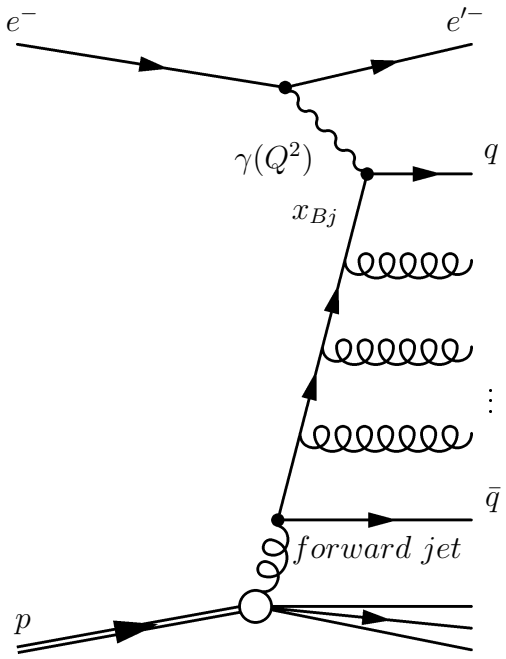

Figure 4.6: Feynman diagram for QCD Compton-like forward jet production.

$\alpha_s \approx 1$ and the series diverges. One is limited in Q^2 to measure extremely low values of x_{Bj}. On the other hand the p_t–cut of the jets combined with the p_t^2/Q^2–cut additionally restricts the phase space for x_{Bj}. If one wants to be independent of the Q^2 constraints, one can use a new scale coming from the relatively large mass of the charm quarks $\mu^2 = 4m_c^2 + p_t^2$. The idea is similar to the *Mueller* jet selection but instead of Q^2 one uses the scale μ^2 for suppressing the DGLAP–like events. The calculations are done at parton level in order to investigate the features and advantages of the use of the new scale μ^2. This is very important in order to study forward jets in photoproduction events, where x_{Bj} and Q^2 can not be used.

In the following a comparison between the two scales Q^2 and μ^2 is presented. The cross section for forward jets as a function of x_{Bj} is shown in figure 4.8. The differential cross section $d\sigma/dx_{Bj}$ using both scales, μ^2 and Q^2 , are in good agreement with each other in shape but not in magnitude. The different values arise since the scale μ^2 is always larger than $9\,\mathrm{GeV}^2$, but Q^2 is limited below by $3\,\mathrm{GeV}^2$. Differences in the shapes are found only in the smallest bin. This effect can be explained from kinematics: x_{Bj} is limited from the variables Q^2 and y (see equation 1.7). With the applied cuts the smallest possible value for x_{Bj} is $x_{Bj} = 0.2 \cdot 10^{-3}$. Since the scale μ^2 does not depend on the cuts for Q^2 and y, there is no restriction in the smallest bin of x_{Bj}.

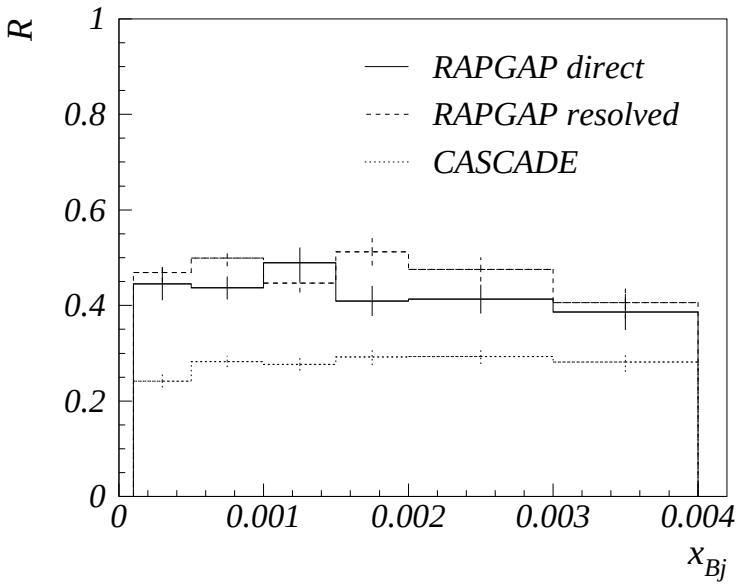

Figure 4.7: *The ratio R as function of the scaling variable x_{Bj}. The solid line presents the result from* RAPGAP *direct, dashed line is* RAPGAP *resolved and dash-dotted line is predictions from* CASCADE . *Predictions from* CASCADE *with negligible mass of the charm quark is denoted with dotted line.*

The Forward Jet Cross Section as a Function of the Hadronic center of Mass energy W

Since Q^2 has a lower limit one is constrained (see equation 1.7) when trying to measure the parton dynamics in regions of small values of the scaling variable x_{Bj}.

The invariant mass of the hadronic final state (see equation 1.4) can be rewritten as a function of x_{Bj} and Q^2:

$$W^2 = Q^2\left(\frac{1-x_{Bj}}{x_{Bj}}\right) \backsim \left.\frac{1}{x_{Bj}}\right|_{fixed\ Q^2} \tag{4.1}$$

For small values of x_{Bj} and fixed Q^2 this equation leads to an inverse proportionality between x_{Bj} and W^2.

In order to investigate the relations and dependences between x_{Bj} and W a fixed value for Q^2 was chosen. The virtuality of the photon Q^2 was set to constant $Q^2 = 25\,\mathrm{GeV}^2$ in both MC generators. The cross section for forward jets as function of both x_{Bj} and W for fixed values of Q^2 are presented in figure 4.9. From the arguments presented above one would expect a cross section increasing at low x_{Bj} also to increase with W^2, but the plots present

the opposite. This can be explained by the Jacobian, where the variable x_{Bj} was changed to W.

$$\frac{d\sigma}{dW} = \frac{d\sigma}{dx_{Bj}} \cdot \frac{dx_{Bj}}{dW}$$

However with a proper variable transformation calculating the Jacobian matrix we get:

$$\frac{d\sigma}{dW} = |2W| \cdot \frac{x_{Bj}}{Q^2 + W^2} \cdot \frac{d\sigma}{dx_{Bj}}$$

The lowest bin for x_{Bj} in figure 4.9 corresponds to the highest bin for W.

In figure 4.10 the cross section for forward jets satisfying $0.5 < p_t^2/\mu^2 < 5$ is shown, as a function of the photon-proton mass W. It is compared with the cross section as function of x_{Bj}. The behavior of both MC models is significantly different and the connection between the two variables x_{Bj} and W is obvious. Therefore W can be used to estimate differences in the evolution ladder.

With the presence of the heavy quarks and applying the new scale $\mu^2 = 4m_c^2 + p_{c,t}^2$ together with replacing x_{Bj} by W the Q^2 cut for DIS can be relaxed and photoproduction of forward jet events can be investigated.

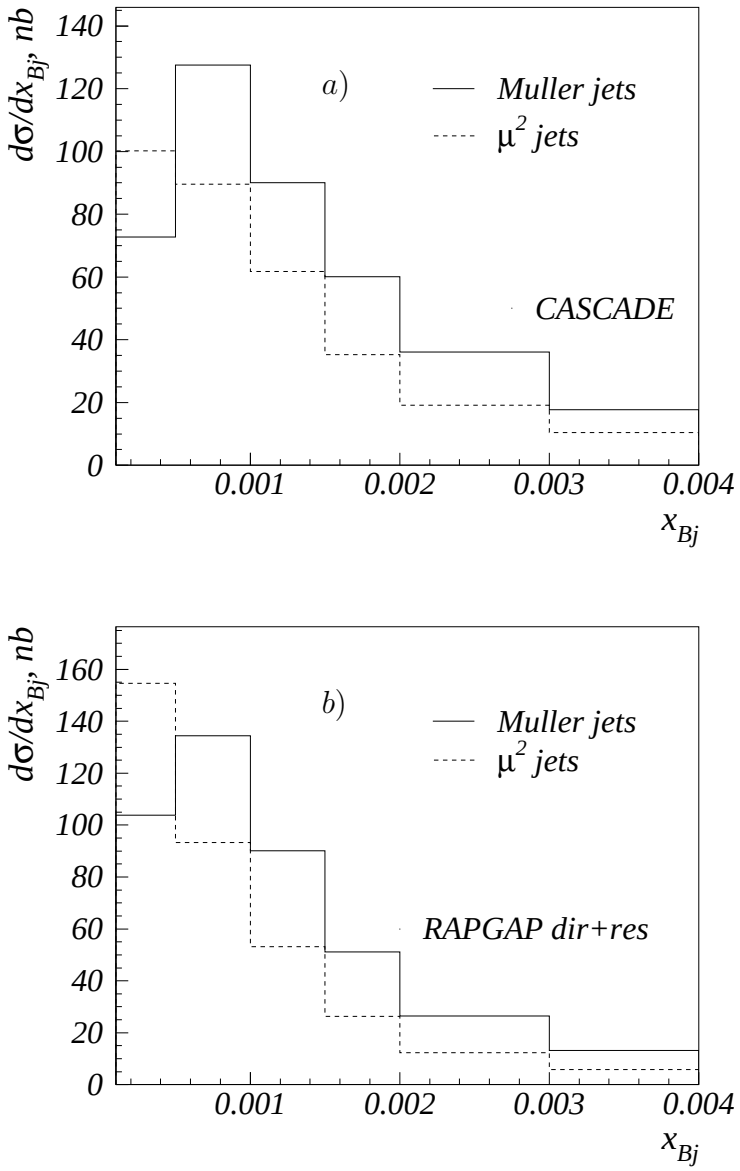

Figure 4.8: *The cross section for forward jets in bins of x_{Bj}. Comparison between different selection criteria for forward jets is presented for two MC models–* CASCADE *and* RAPGAP *in a) and b) respectively. The dashed line represents the μ^2 hard scale and the solid line represents Q^2.*

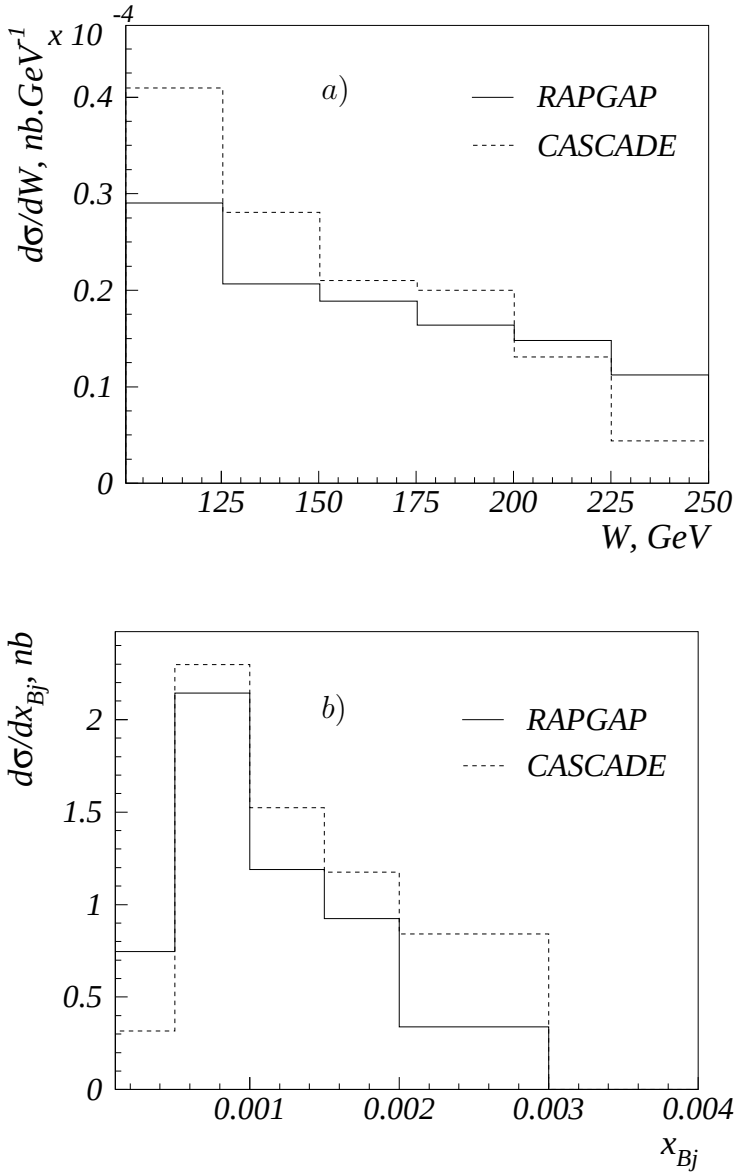

Figure 4.9: *The cross section for forward jets in bins of* W *and* x_{Bj} *in* a*) and* b*) respectively in DIS with* $24.5\,\mathrm{GeV}^2 < Q^2 < 25.5\,\mathrm{GeV}$*. The dashed line presents prediction from* CASCADE *and the solid line is* RAPGAP*. The forward jets were selected with the* p_t^2/μ^2 *cut.*

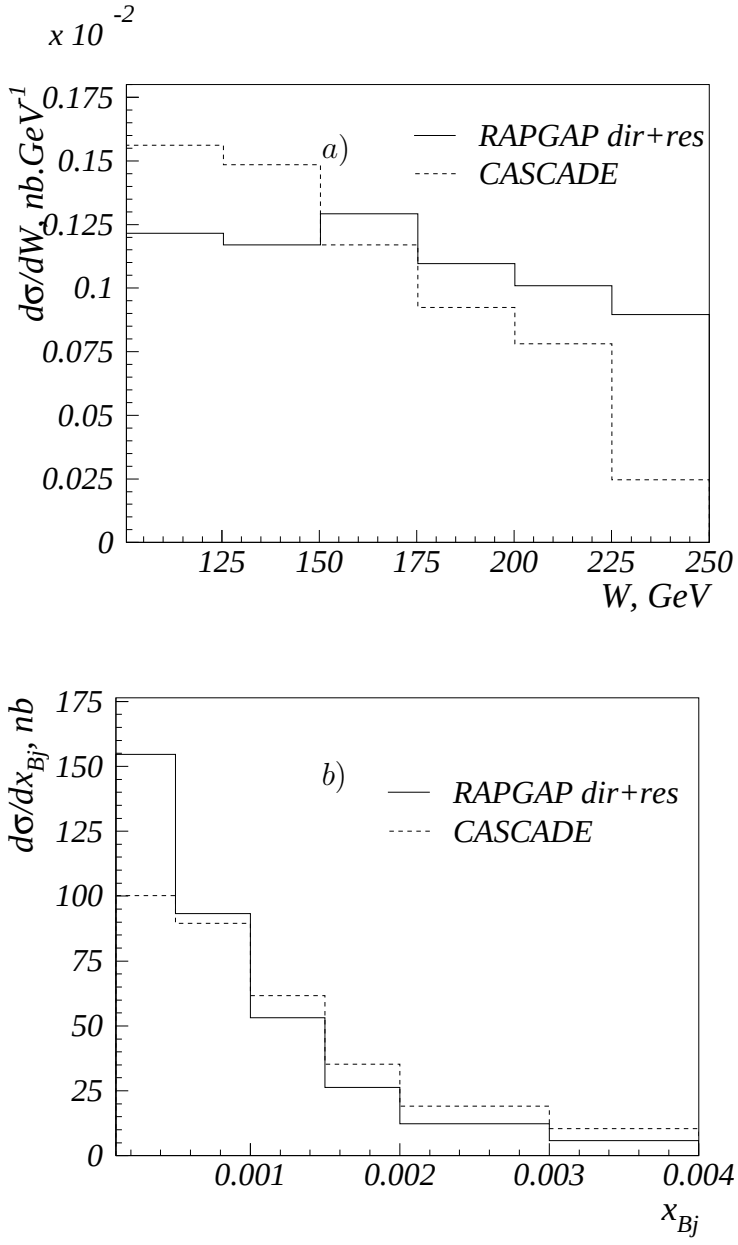

Figure 4.10: *The cross section for forward jets in DIS in bins of* W *a) and* x_{Bj} *b) is presented. The solid line presents results from* RAPGAP *and the dashed line presents results from* CASCADE.

Chapter 5

Forward Jets in Charm Photoproduction

In the previous chapter a Monte Carlo (MC) investigation on forward jet events with and without tagging of a charm quark in DIS was presented. The forward jets were selected in two different ways: applying p_t^2/Q^2 and p_t^2/μ^2 cuts. The scale μ^2 depends on the kinematic of the charm quarks and it is defined via the following relation $\mu^2 = 4 \cdot m_c^2 + p_t^2$. In the previous chapter it was shown that the Bjoerken variable x_{Bj}, which is not defined in photoproduction, can be replaced by the invariant mass of the hadronic system, W. The latter was used as a sensitive variable to highlight the differences between ordered and unordered parton emission. It was shown, that it is possible to soften the Q^2 cut and to investigate photoproduction of forward jets. In this chapter results from MC studies on forward jets in charm photoproduction are presented.

5.1 Forward Jet and Double Charm Correlation

With the kinematic quantity Q^2 two different regimes in electron–proton scattering can be separated: when the virtuality of the photon is small $Q^2 \lesssim 1\,\mathrm{GeV}^2$, the regime is called *photoproduction* and when it is larger, $Q^2 \gtrsim 1\,\mathrm{GeV}^2$ *Deep Inelastic Scattering (DIS)*. In DIS large Q^2 ensures small values of α_s and perturbative calculations can be applied. In photoproduction small values of α_s are ensured when objects like jets or heavy quarks are required. Their kinematic quantities, e.g. mass and transverse momenta, can be used as hard scales so that perturbative calculations converge and give reliable predictions.

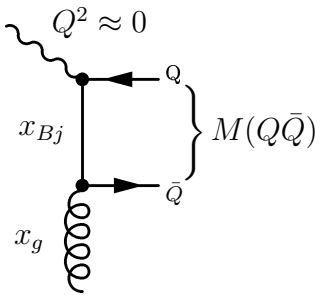

Figure 5.1: *Schematic Feynman diagram on parton level for heavy quark photoproduction via boson-gluon fusion process.*

When the virtuality of the photon Q^2 vanishes the kinematical variable x_{Bj} is not defined. However the quantity x_g, the longitudinal momentum fraction of the incoming gluon participating in the hard interaction, can be defined:

$$x_g = \frac{M^2(Q\bar{Q}) + Q^2}{y \cdot s} = x_{Bj} + \frac{M^2(Q\bar{Q})}{y \cdot s} = \approx \frac{M^2(Q\bar{Q})}{y \cdot s}\Big|_{Q^2 \longrightarrow 0} \tag{5.1}$$

Here M is the invariant mass squared of the quark-antiquark pair, $\sqrt{s}$ represents the center-of-mass energy and y is the Bjoerken variable (see figure 5.1). With HERA energies and the highest possible value of y, $y = 1$, the minimum value of x_g for photoproduction of charm quarks is $x_g \approx 10^{-4}$. Photoproduction provides access to the small x_g regions. Using equation 1.8 and neglecting the virtuality of the photon equation 5.1 can be rewritten:

$$x_g = \frac{M^2(Q\bar{Q})}{W^2} \tag{5.2}$$

For fixed values of the invariant mass of the quark pair there is an inverse proportionality between x_g and W: large values of W lead to small values of x_g.

In order to define x_g both charm quarks have to be reconstructed or both jets have to be tagged. Since this is a difficult procedure one needs new observables. In photoproduction equation 5.2 is dominated by small values of M^2. The charm quarks are created close to the mass threshold. Hence there is still proportionality between x_g and W. In addition to small values of x_g small values for the rapidity difference between the charm quarks in the quark box are expected. For this reason, the relevant quantities in charm

photoproduction are the invariant mass of the *Hadronic Final State* (HFS), W, and rapidity differences between the forward jet and the charm quarks.

In analogy with the DIS case (see chapter 4 and figure 4.1), a forward jet can be defined in photoproduction as well. If relatively large values of x_{jet} are required and small values of x_g, the phase space is open for an evolution in x. The DGLAP–type evolution can be suppressed in the presence of the charm quarks and by using the scale $\mu^2 = 4m_c^2 + p_t^2 \gtrsim 9\,\mathrm{GeV}$. In addition the large transverse momentum of the forward jet provides enough phase space where perturbative calculations can be applied.

Since the total cross section is proportional to $1/Q^4$ the photoproduction regime provides large enough statistics to investigate charm events with forward jets.

Results

In this chapter two MC generators are used for the predictions: RAPGAP version 3.01 and CASCADE version 1.2. In RAPGAP the DGLAP evolution is used to compute the initial state parton showering. Two different processes are generated separately and added afterwards: direct photon-gluon fusion and resolved photon processes including heavy quarks. The parton density parameterizations used are CTEQ5HQ1 for the proton and GRS–G LO for the photon. In contrast the CCFM evolution equation is used in CASCADE and no resolved photon processes are considered explicitly.

In order to investigate various models and to define observables which are relevant to distinguish different parton evolution schemes the studies are done on the parton level. All gluons and quarks are taken into account.

A cut on the photon virtuality, $Q^2 < 0.1\,\mathrm{GeV}^2$, limits the analysis to the photoproduction regime. The inelasticity is restricted to $0.1 < y < 0.8$. The charm quarks were selected when they lie in the central rapidity range $|\eta^c| < 2$. Forward jets are selected in the following way. They were defined by using the k_t algorithm and were build up from the partons in the final state. Jets with transverse momenta $p_t^{jet} > 3.5\,\mathrm{GeV}$, longitudinal momentum fraction $x_{jet} = E_{jet}/E_p > 0.035$ and rapidities in the range $1.736 < \eta^{jets} < 2.794$ are selected and in the following referred to as *forward jets*. The cut on x_{jet} opens up the phase space for evolution in x. An additional p_t cut defined by the kinematics of the charm quarks, $0.5 \cdot \mu^2 < p_t^2 < 5 \cdot \mu^2$ is applied. Jets which fulfill this additional requirement on p_t^2/μ^2 which suppresses the DGLAP–like evolution are called *Mueller jets*. The cuts are summarized in table 5.1.

In figures 5.2–5.4 the cross section for forward jet and *Mueller* jet is presented as a function of ${p_t}^{jet}$, η and E. For these quantities the two different

Q^2	$Q^2 < 0.1\,\mathrm{GeV}^2$
y	$0.1 < y < 0.8$
p_t^{jets}	$p_t^{jets} > 3.5\,\mathrm{GeV}$
η^{jets}	$1.736 < \eta^{jets} < 2.794$
x_{jet}	$x_{jet} > 3.5$
η^c	$\lvert\eta^c\rvert < 2$
p_t^2/μ^2	$0.5 < p_t^2/\mu^2 < 5.$

Table 5.1: *Table with the main cuts defining the visible range.*

criteria do not reveal any significant differences. In the η spectra it can be seen that the rapidity of the *Mueller* jets shows a steeper behavior than the forward jets in the most forward region. The three models agree with each other in shape but not in magnitude. CASCADE predicts larger cross section than the direct component of RAPGAP. Only if the resolved component is added to the cross section reasonable agreement is achieved although RAPGAP is still below CASCADE. From these distributions one can conclude that the p_t^2/μ^2 cut makes no effect. This is obvious since both– p_t^2 and μ^2– are limited from below by 9 GeV. Finally this cut rejects only jets of momenta $p^2 > 5\mu^2$ which have a smaller cross section.

On picture 5.5 the cross section as a function of the mass of the hadronic system W is presented for the two methods. CASCADE has a steeper slope with increasing W than RAPGAP (even when adding direct and resolved components). In figure 5.5 *b*) where the p_t^2/μ^2 cut was applied a slight difference between the two models is found. However, the difference is not pronounced enough to draw any conclusion.

In figure 5.6 the cross section for a *Mueller* jet in charm photoproduction as a function of the rapidity difference between the *Mueller* jet and the charm quark $\Delta\eta$ is presented. Only one charm quark in the *visible range* (see table 5.1) is required. The largest cross section is observed in the smallest and medium $\Delta\eta$ bins. The forward jet is mainly found in the rapidity region between $2.3 \lesssim \eta \lesssim 2.8$ (figure 5.3 *b*)), therefore the rapidity of the charm quark can be considered to lie in the central η region. For example, if $\eta^{fwd} \approx 2.5$ and $\Delta\eta \approx 2$ the rapidity of the charm quark should be $\eta^c \approx 0.5$. However values for $\Delta\eta$ at $\Delta\eta \approx 4$ are still possible. The charm may be found in the most backward direction.

When an additional charm quark to the charm–*Mueller* jet pair is required the three objects were ordered in rapidity $\eta^{c_1} < \eta^{c_2} < \eta^{fwd}$, $\eta_{c_{1(2)}}$ is the pseudo rapidity of the charm quarks and η_{fwd} presents the rapidity of the *Mueller* jet. The rapidity difference between the charm quarks is labeled $\Delta\eta'$. The

distribution of $\Delta\eta$ is separated in two regions: where $\Delta\eta\prime$ is greater and smaller than one. In this scenario the rapidity difference $\Delta\eta$ is defined as the difference between the charm which is *closest* in rapidity space to the *Mueller* jet $\Delta\eta = |\eta_{c_2} - \eta_{fwd}|$.

In figure 5.7 *a*) and *b*) the differential cross section for *Mueller* jets and two charm quarks in the acceptance as a function of $\Delta\eta$ for different bins of $\Delta\eta\prime$ ($\Delta\eta\prime < 1$ and $\Delta\eta\prime \geq 1$ respectively) is presented. In figure 5.7 *a*), in the region where $\Delta\eta$ is large the difference between RAPGAP and CASCADE becomes significant. When $\Delta\eta\prime$ is small the invariant mass of the quark pair is small. Thus small values of x_g are expected. In RAPGAP this case is highly suppressed due to p_t ordering in the model in contrast to CASCADE where the small values of x_g are favored. Although there is a difference in magnitude between the two models, both show that the rapidity difference between the *Mueller* jet and the charm anti-charm system is mainly between $\Delta\eta \approx 1$ to 3. In figure 5.7 *b*) the differences become not so large although RAPGAP is below CASCADE. For very large values of $\Delta\eta \approx 4$ no phase space is left and the cross section vanishes (the $\Delta\eta\prime$ requirement additionally restricts it). These values correspond to rapidity of the *closest* charm of $\eta_{c2} \approx -1$.

In figure 5.9 the differential cross section as function of the rapidity difference $\Delta\eta$ is shown. A comparison between direct and resolved photoproduction as calculated by RAPGAP is presented. This figure aims to show the contribution of the so called *charm excitation* process: when the quasi real photon splits into a charm-anti charm quark pair and one of them enters the hard scattering (see figure 4.3), the charm *absorbs* the gluon from the proton. In figure 5.9 one can see that the resolved component is negligible when charm excitation is not considered.

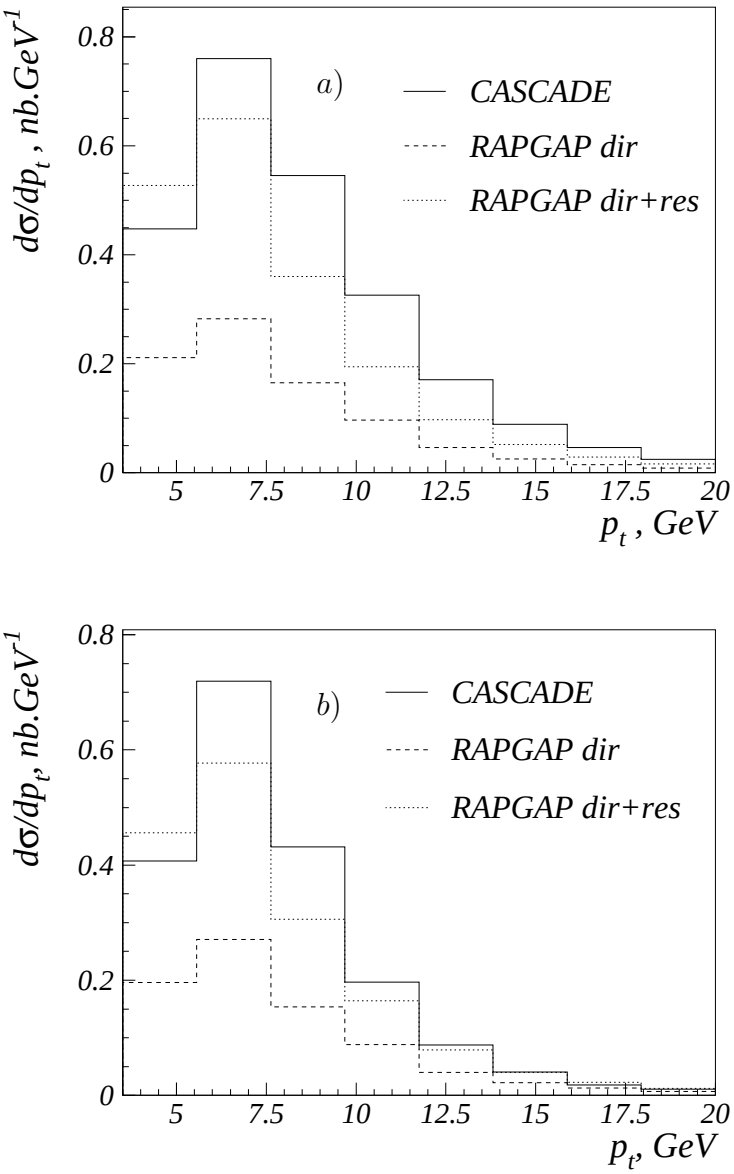

Figure 5.2: *The cross section for forward jets defined in two ways: (a) without and (b) with the restriction* $0.5 < p_t^2/\mu^2 < 5$. *as a function of the transverse momentum of the jets. The predictions from* CASCADE *are labeled with a solid line and predictions from* RAPGAP *with dashed and dotted line for direct and the sum of direct and resolved photons respectively.*

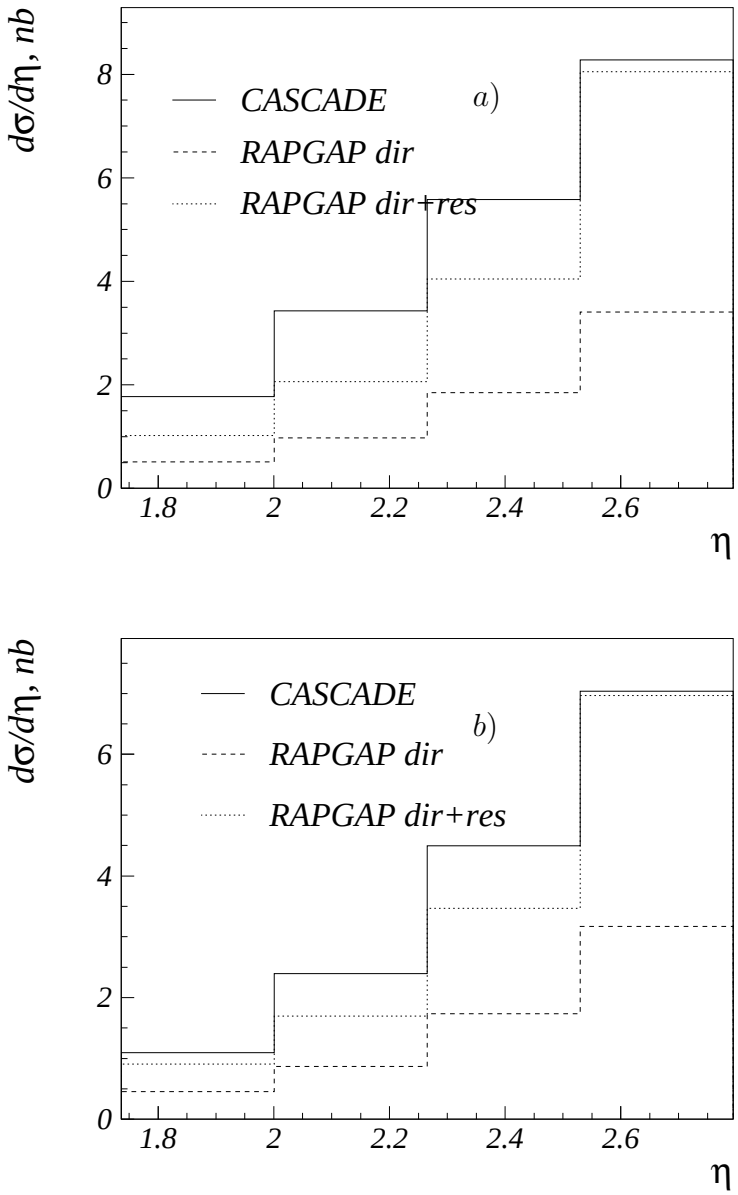

Figure 5.3: *The cross section for forward jets defined in two ways: (a) without and (b) with the restriction* $0.5 < p_t^2/\mu^2 < 5$. *as a function of the pseudo rapidity of the jets. The predictions from* CASCADE *are labeled with a solid line and predictions from* RAPGAP *with dashed and dotted line for direct and the sum of direct and resolved photons respectively.*

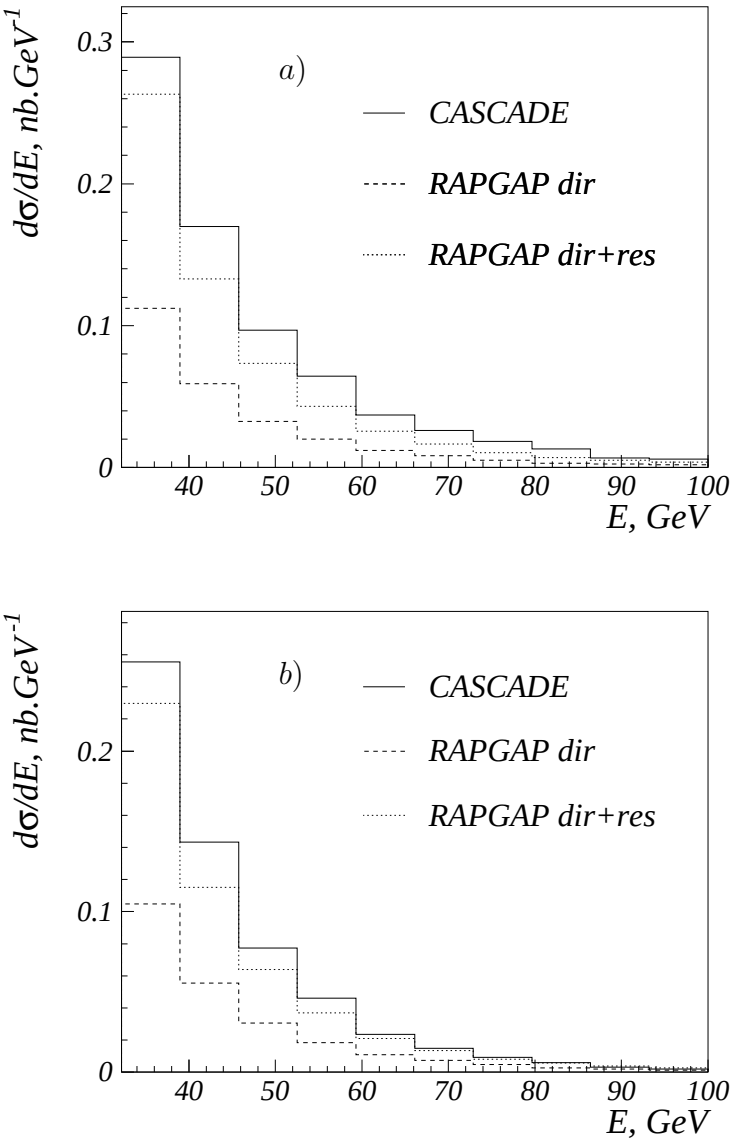

Figure 5.4: *The energy spectra for (a) forward jets and (b) Mueller jets.*

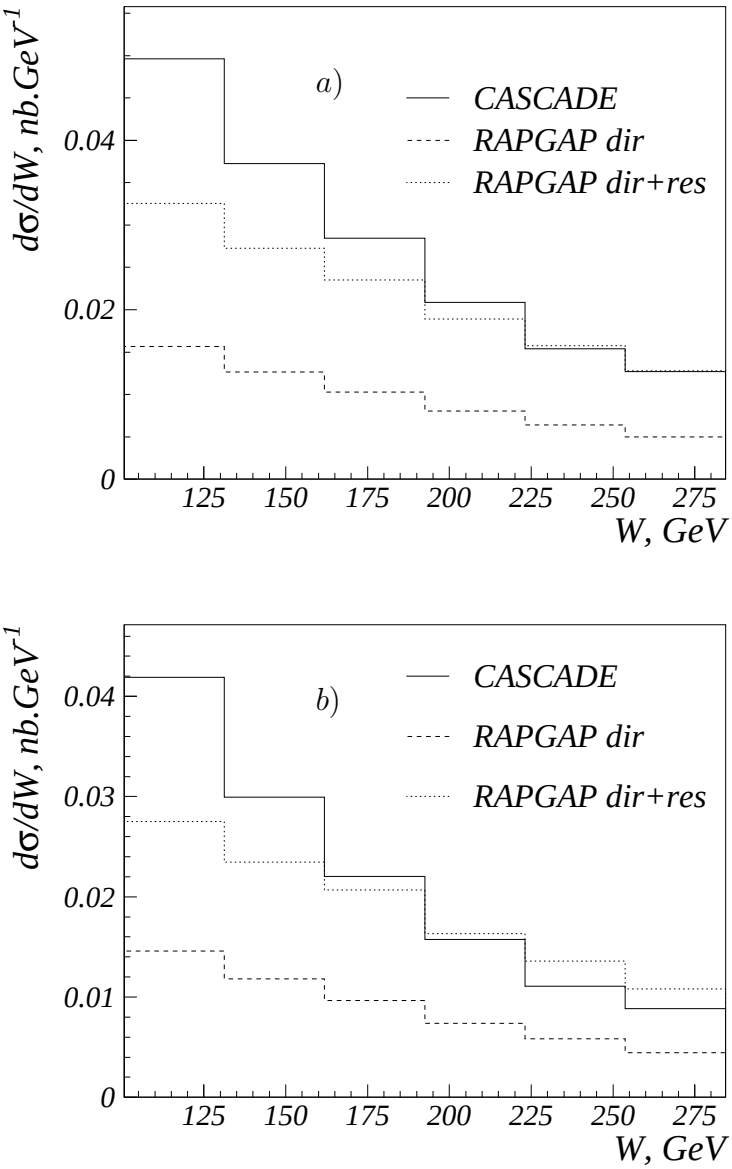

Figure 5.5: *The cross section for forward (a) and* Mueller *jets (b) in bins of* W. *Results from* CASCADE *and* RAPGAP *are labeled with solid and dashed lines respectively. The dotted line represents the sum of the direct and resolved component of the program.*

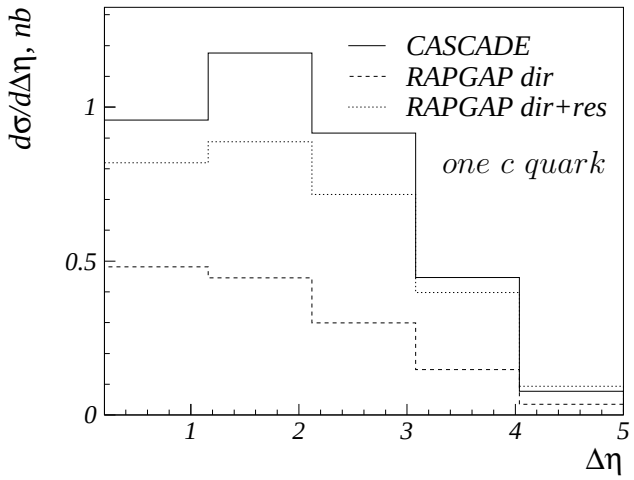

Figure 5.6: *The cross section for Mueller jets in bins of* $\Delta\eta = |\eta^{c_2} - \eta^{fwd}|$ *when one charm is found in the acceptance.*

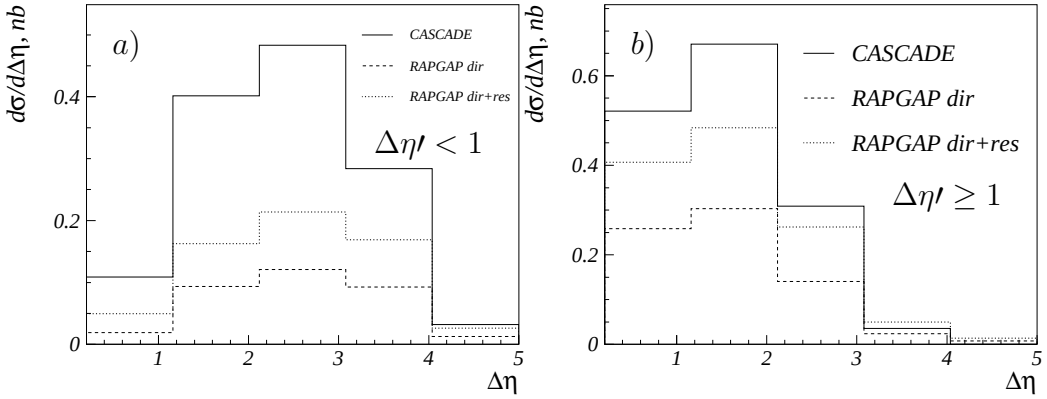

Figure 5.7: *Rapidity difference between forward jet and a charm quarks in events where two charm quarks are found. Pictures a) and b) shows results when the following cases were considered:* $\Delta\eta' < 1$ *and* $\Delta\eta' > 1$ *respectively. The solid line presents calculations from* CASCADE, *dashed line resolved and dotted line direct photon, both from* RAPGAP.

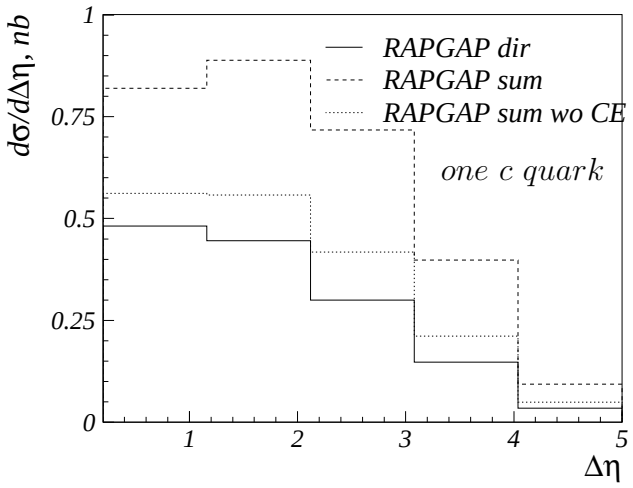

Figure 5.8: *The differential cross section for Mueller jets and one charm quark in the acceptance $d\sigma/d\Delta\eta$. Comparison between direct (solid line) and sum with resolved components of* RAPGAP *with and without charm excitation (dashed and dotted line).*

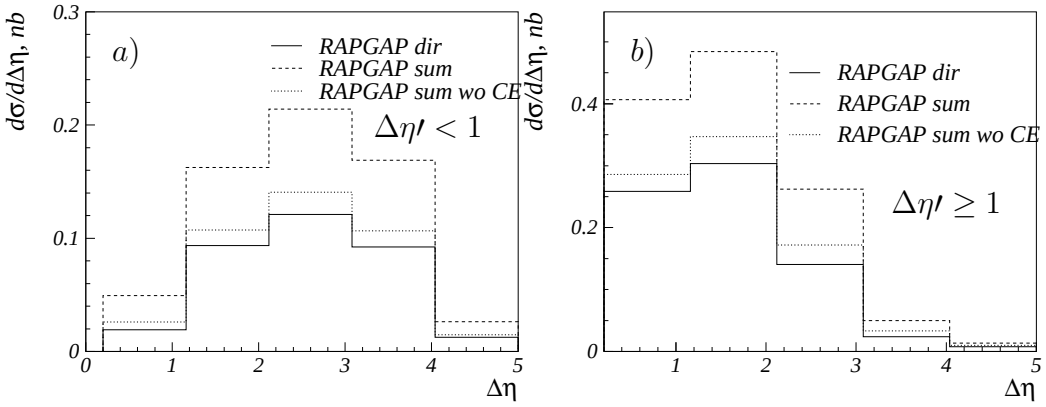

Figure 5.9: *The cross section for jets as function of the rapidity difference between the closest charm and the jet. Pictures a) and b) presents this cross section for different values of $\Delta\eta'$: $\Delta\eta' < 1$ and $\Delta\eta' > 1$ respectively as predicted by* RAPGAP.

5.2 Forward Jet and D^*

In the previous section a MC investigation on forward jets with double charm correlations in photoproduction was presented. It was shown that the observable W can be used to distinguish differences in parton evolution schemes. In addition to W the rapidity differences between the charm quarks and the forward jets can also reveal different behavior of the shape and the magnitude of the cross section. Since the partons are confined one is not able to observe them before they hadronise into observable hadrons or jets. In this section a MC investigation of a forward jet in addition to the D^* meson is presented.

All the D^* mesons were selected within the *visible range* (see table 5.2) and no branching ratio was taken into account. The cross section for photoproduction of D^* meson was calculated in the kinematic region of $0.1 < y < 0.8$. The D^* is required to satisfy: $p_t^{D^*} > 2\,\text{GeV}$ and $|\eta^{D^*}| < 1.5$. These cuts correspond to the H1 detector acceptance and resolution (see chapter 6). The jet, to which the D^* belongs was defined as described in chapter 3. In addition to the D^*–jet a second jet was required in the forward region. All the jets were demanded to have transverse momentum $p_t^{jet} > 3.5\,\text{GeV}$. The forward jet is defined as in the previous section (5.1). All D^* and jet cuts are listed in table 5.2.

Phase Space Cuts

Q^2	$Q^2 < 0.1\,\text{GeV}^2$
y	$0.1 < y < 0.8$

D^* Cuts

$p_t^{D^*}$	$p_t^{D^*} > 2\,\text{GeV}$
η^{D^*}	$\lvert\eta^{D^*}\rvert < 1.5$

Jet Cuts

p_t^{jets}	$p_t^{jets} > 3.5\,\text{GeV}$
η^{jets}	$-1.5 < \eta^{jets} < 2.794$

Forward Jet Cuts

$\eta^{fwd\ jet}$	$\eta^{fwd\ jet} > 1.736$
x_{jet}	$x_{jet} > 0.035$

Mueller Jets

p_t^2/μ^2	$0.5 < p_t^2/\mu^2 < 5.$
μ^2	$\mu^2 = 4 \cdot m_{D^*}^2 + p_t^{D^*,2}$

Table 5.2: *Summary of the cuts applied on D^* and the jets defining the visible range.*

The cross sections in this visible range for D^*, forward jets and *Mueller* jet as predicted by RAPGAP– direct, the sum of the resolved and the direct component and CASCADE are given in table 5.3. In the calculation of the cross section for the resolved component the charm quarks are treated massless. Therefore the total cross section for RAPGAP(direct and resolved) is larger than that predicted by CASCADE. After the cuts are applied the cross section becomes smaller for RAPGAP.

Total Cross Section ($ep \longrightarrow ec\bar{c}X$)

CASCADE	224.593 nb
RAPGAP direct	208.912 nb
RAPGAP direct+resolved	348.796 nb

Cross Section for $D^*(ep \longrightarrow eD^*X)$

CASCADE	23.326 nb
RAPGAP direct	13.117 nb
RAPGAP direct+resolved	24.562 nb

Forward Jet Cross Section ($ep \longrightarrow eD^* + forward\ jet$)

CASCADE	95.699 pb
RAPGAP direct	88.024 pb
RAPGAP direct+resolved	68.497 pb

Mueller jet cross section ($ep \longrightarrow eD^* + Mueller\ jet$)

CASCADE	71.892 pb
RAPGAP direct	32.946 pb
RAPGAP direct+resolved	61.136 pb

Table 5.3: *Cross sections predicted for charm photoproduction with* RAPGAP *and* CASCADE.

In figure 5.10 the p_t and η spectra of the D^* are presented. The predictions from CASCADE are significantly larger than the direct component of RAPGAP. When the resolved contribution is added to the latter no significant difference is observed between the two models. Differences between figures 3.1 *a*) and 5.10 *a*) as well as between 3.3 *a*) and 5.10 *b*) are observed. This is due to different phase space cuts– the Bjoerken variable y was changed from $0.29 < y < 0.65$ (in chapter 3) to $0.1 < y < 0.9$.

In analogy to the previous section a comparison between forward jet and *Mueller* jet cross sections is performed. In figures 5.11 and 5.12 the differential cross section for a forward and a *Mueller* jet in bins of p_t and η is shown. The differential distribution in figure 5.11 is broader for the forward than for the *Mueller* jets. In plot 5.11 *b*) it can be seen that the momentum of the

jets is concentrated in the range $5\,\mathrm{GeV} \lesssim p_t\,\mathrm{GeV} < 11\,\mathrm{GeV}$. For these distributions no significant difference between RAPGAP and CASCADE is found.

In figure 5.2 the cross section for forward *a*) and *Mueller* jets *b*) in bins of W is presented. The shape of the distribution for RAPGAP does not change after the p_t^2/μ^2 cut is applied but only the magnitude. In contrast CASCADE reveals a steeper W distribution when the cut is applied.

Having selected the D^* meson and the *Mueller* jet, it is possible to investigate their difference in transverse momentum $\Delta p_t = \mathbf{p}_t^{D^*} - \mathbf{p}_t^{fwd\ jet}$. They have to be balanced $\mathbf{p}_t^{D^*} = -\mathbf{p}_t^{fwd\ jet}$ (see chapter 3) if no additional radiation occurs. In figure 5.14 the differential distribution $d\sigma/d\Delta p_t$ is presented. The solid line corresponds to predictions from CASCADE, the dashed line and the dotted are the direct and resolved components of RAPGAP, respectively. Both components of RAPGAP give a narrow distribution of Δp_t, peaked at $\Delta p_t \approx 2$. In contrast, the CASCADE predictions are broader and shifted to a peak at $\Delta p_t \approx 4$. In the latter model additional gluon radiation is more likely than in RAPGAP, which leads to these differences. The peaks are not located around $\Delta p_t \approx 0$ since the p_t cuts for jets and D^* are not the same: $p_t^{D^*} > 2\,\mathrm{GeV}$ and $p_t^{jet} > 3.5\,\mathrm{GeV}$. The difference between them agrees with the position of the peak in RAPGAP.

The rapidity difference between the *Mueller* jet and the D^* is defined $\Delta\eta = \eta^{D^*} - \eta^{jet}$. In figure 5.15 the differential cross section $d\sigma/d\Delta\eta$ for *Mueller* jets is presented. The distribution is peaked at $\Delta\eta \approx -2$ which corresponds to a rapidity of the D^* in the central region $|\eta^{D^*}| < 0.5$ since the *Mueller* jet has rapidity $\eta \approx 2.7$. When the resolved component is included in RAPGAP reasonable agreement between both models is found in the region $\Delta\eta < -2.7$ where the D^* is found in the most backward direction. For larger rapidity difference RAPGAP is clearly below CASCADE which shows that the different parton emissions in the models have a sizeable effect.

In figure 5.16 differential cross sections as a function of $\Delta\phi = |\eta^{D^*} - \eta^{jet}|$ are presented. Significant differences between the models are found. Both components of RAPGAP are peaked at $\Delta\phi \approx \pi$ and steeply falling towards smaller values. For $\Delta\phi < 2$ the resolved component has negligible contribution to the total cross section of RAPGAP. In contrast CASCADE falls less steeply towards smaller $\Delta\phi$. Due to additional gluon radiation included in the model a large decorrelation in azimuthal angle is observed.

In figure 5.17 the cross section for a D^*, a *Mueller* jet and one or two (5.17 *a*) and 5.17 *b*)) additional jets in the visible range is presented. When one additional jet is required the shapes of the predictions become similar in contrast to figure 5.16. However CASCADE is still significantly above the RAPGAP (direct and resolved)prediction. It is also visible that the resolved component contributes mainly to $\Delta\phi > 2$. The peak is displaced toward

smaller values of $\Delta\phi \approx 2.7$. In figure *b*) the $\Delta\phi$ distribution is presented, where two additional jets to the D^*–*Mueller* jet pair was required. The cross section given by RAPGAP is very small while CASCADE is orders of magnitude larger.

In figures 5.15 and 5.16 the cross section for D^* and *Mueller* jets in bins of $\Delta\eta$ and $\Delta\phi$ is presented. The regions where the resolved component has significant contribution is at medium values of $\Delta\eta$ and large values of $\Delta\phi$: $-3.5 < \Delta\eta < -1.5$ and $\Delta\phi > 2$ respectively. Therefore when the D^* meson is found in the central region in η the D^* meson and forward jet are well correlated in $\Delta\phi$ and no significant further gluon emission is observed. In the large rapidity difference (when the D^* meson is in the most backward direction) the correlation in $\Delta\phi$ is violated.

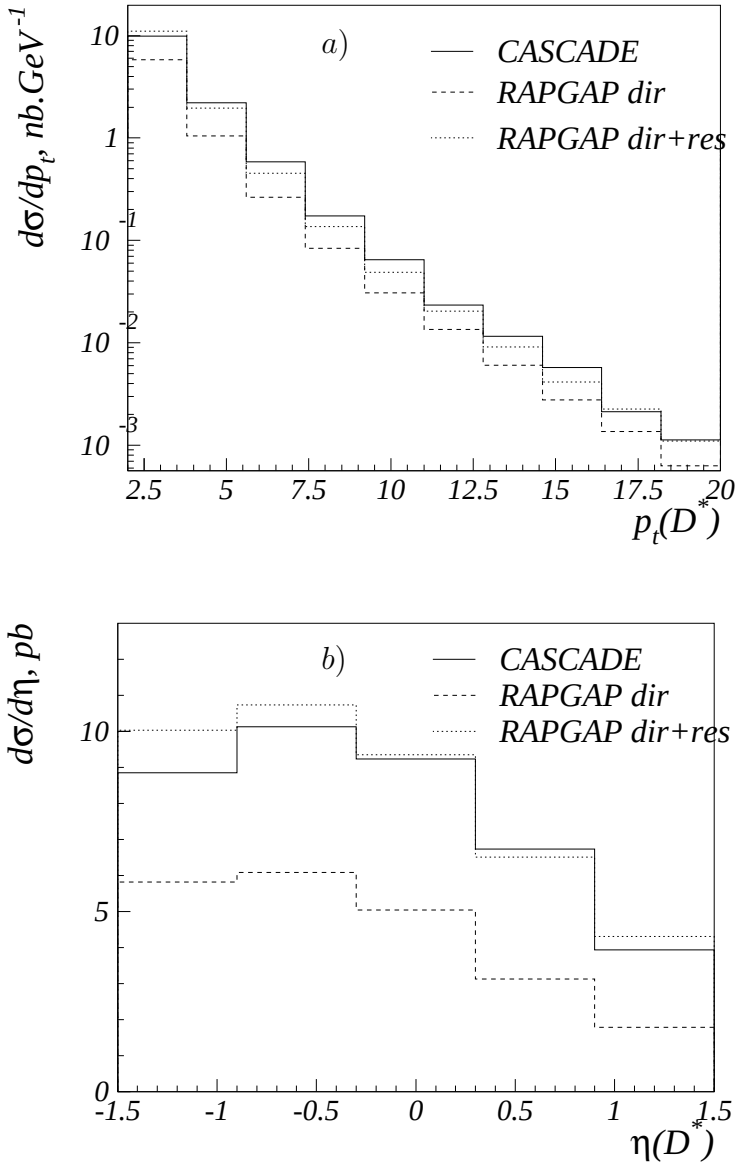

Figure 5.10: *The differential cross section $d\sigma/dp_t$ (a) and $d\sigma/d\eta$ (b) for inclusive D^* meson photoproduction. The solid line presents predictions from* CASCADE, *dashed and dotted line presents* RAPGAP *direct and sum over direct and resolved components respectively.*

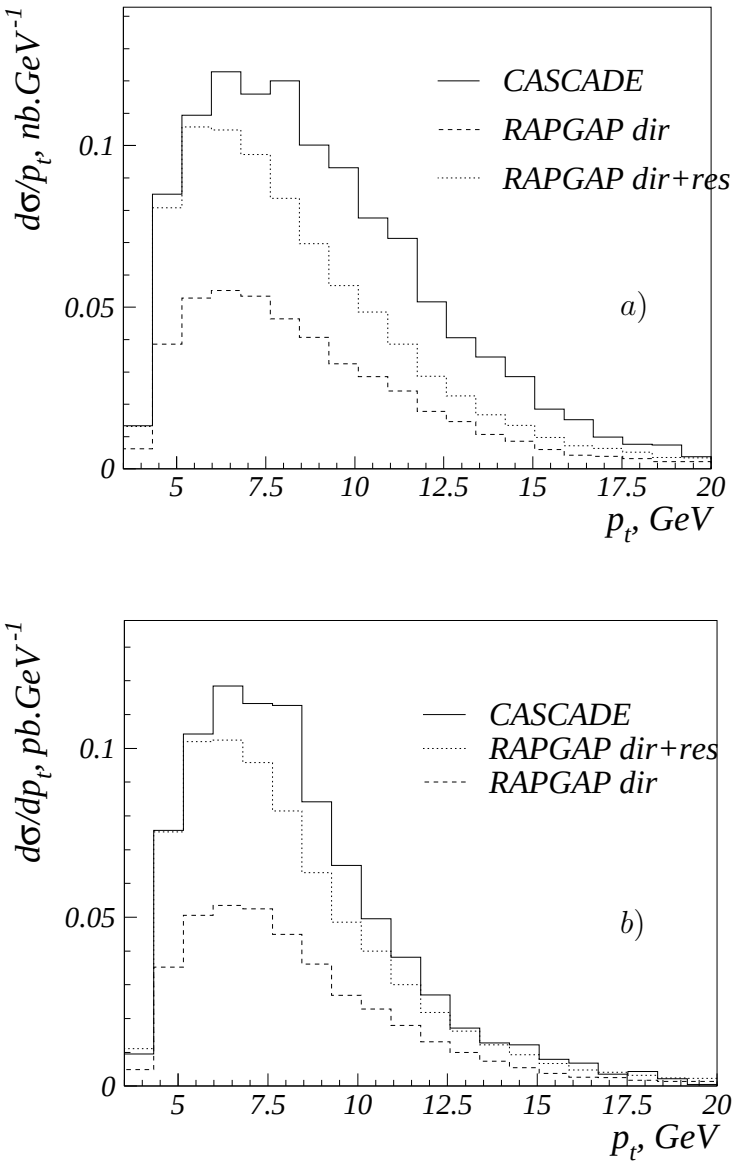

Figure 5.11: *The cross section for forward a) and Mueller jet b) as a function of p_t. The solid line presents the predictions from* CASCADE, *dashed and dotted line presents* RAPGAP *direct and sum over direct and resolved components respectively.*

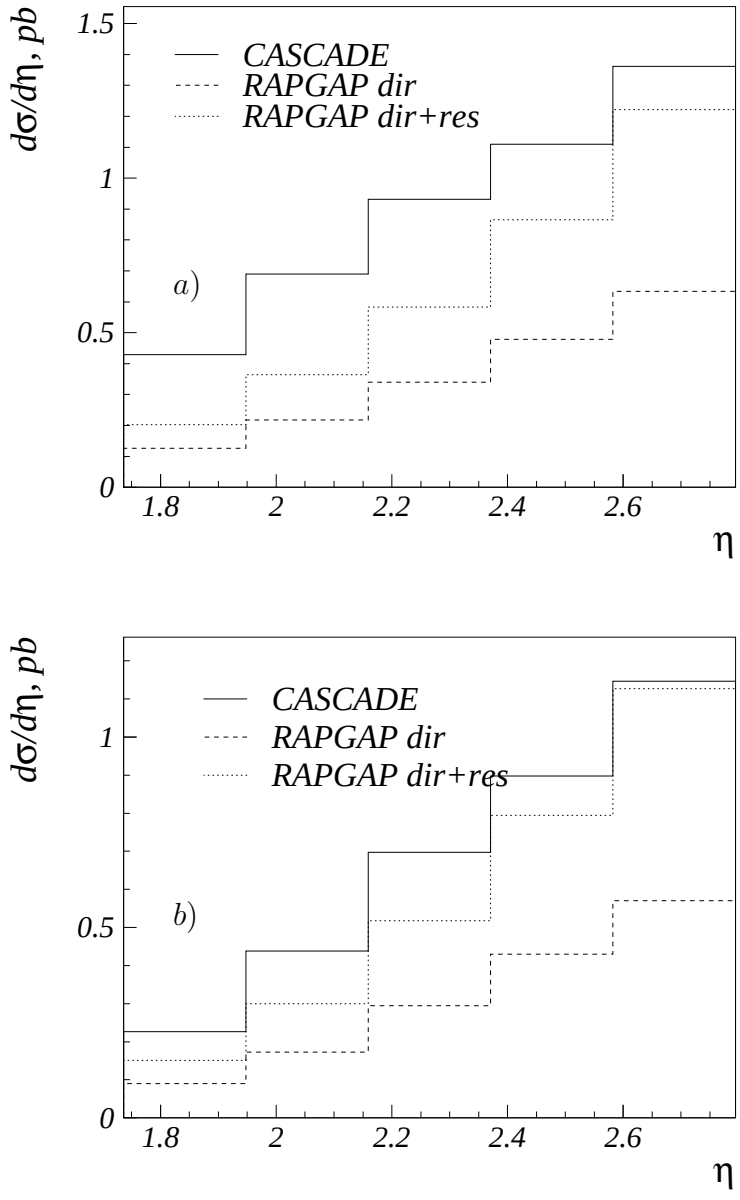

Figure 5.12: *The differential cross section $d\sigma/d\eta$ in bins of η for forward and Mueller jet on a) and b) respectively.*

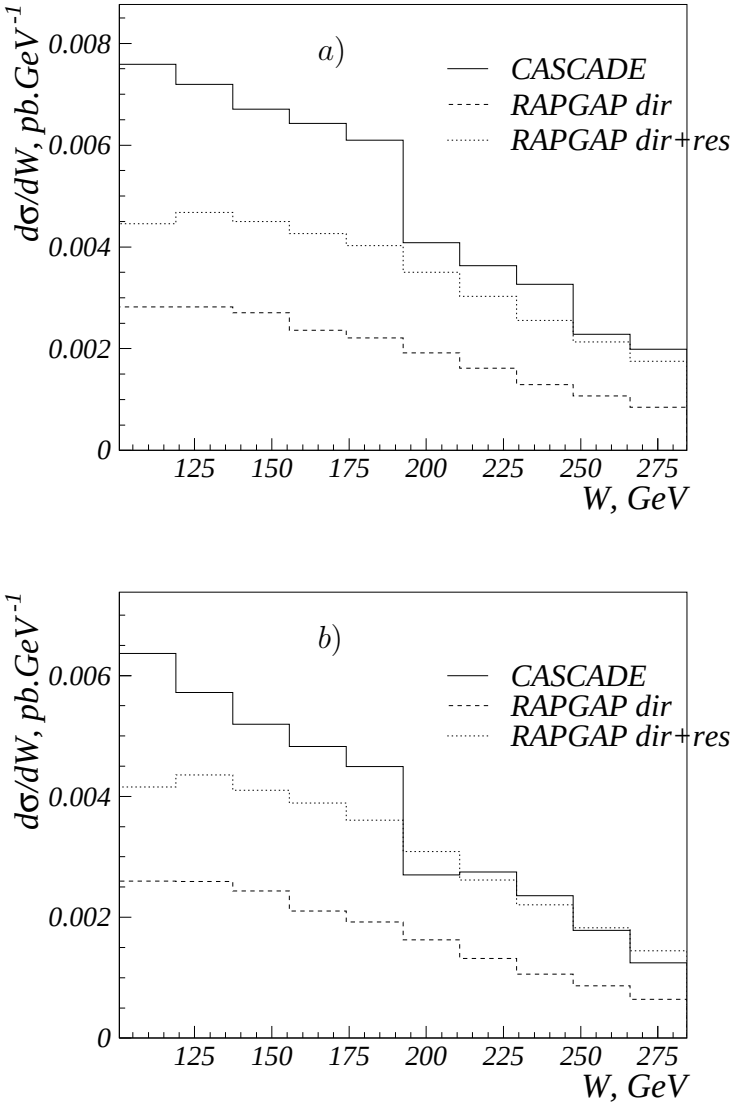

Figure 5.13: *The cross section for forward and Mueller jet as a function of W on a) and b) respectively.*

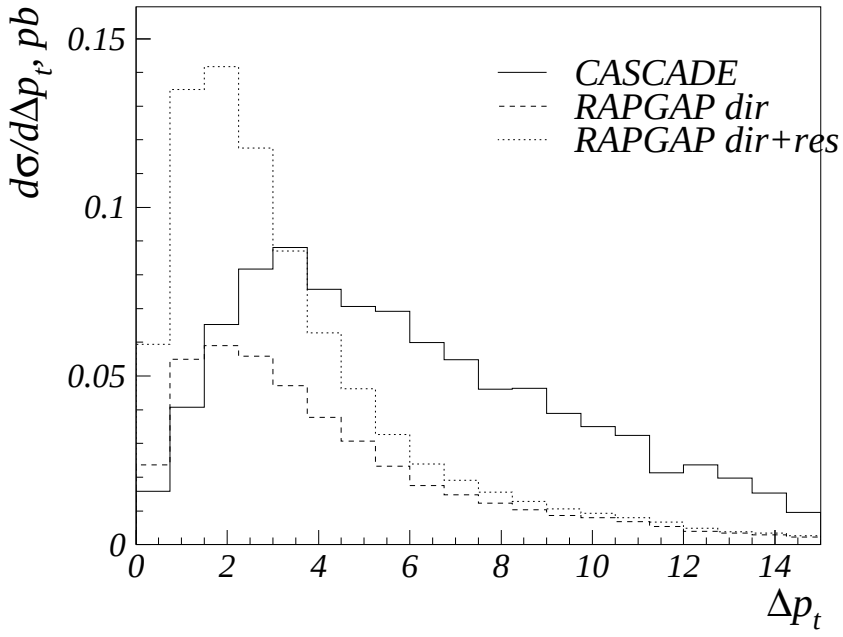

Figure 5.14: *The cross section for Mueller jet in bins of Δp_t. Predictions from* CASCADE *are labeled with the solid line while* RAPGAP *calculations are labeled with dashed and dotted line for the direct and for the sum of direct and resolved respectively.*

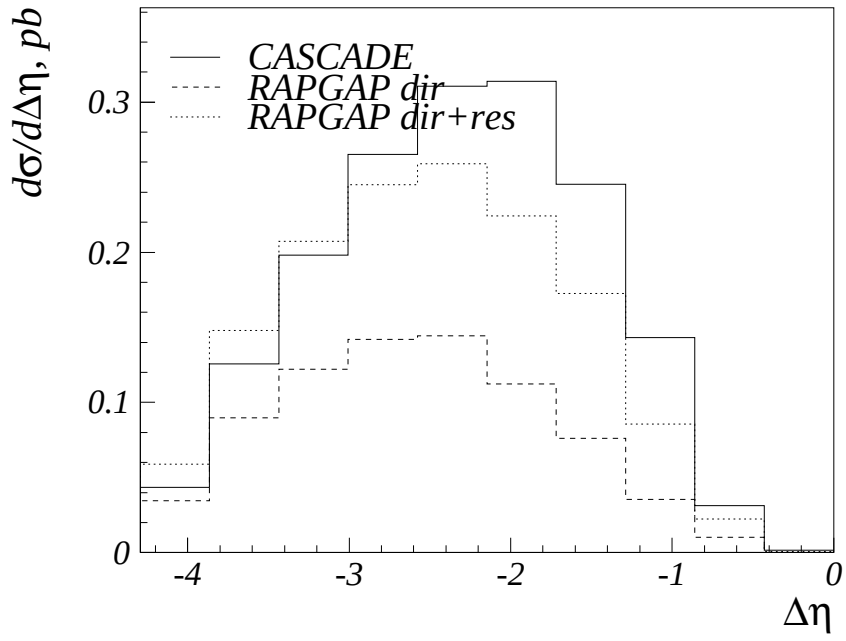

Figure 5.15: *The differential distribution $d\sigma/d\eta$ for Mueller jet production as calculated by* CASCADE *(solid line),* RAPGAP– *direct photoproduction (dashed line) and sum over direct and resolved components (dotted line).*

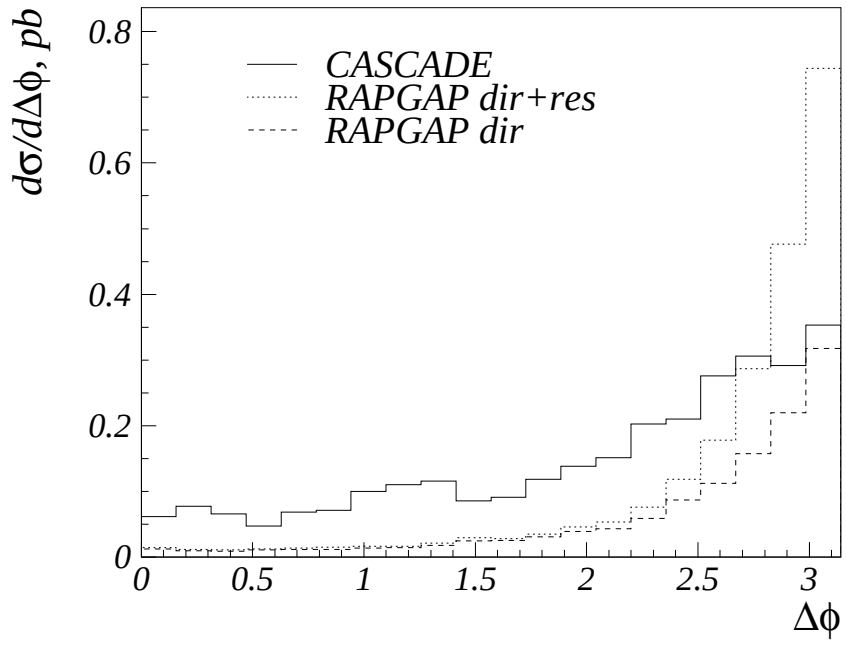

Figure 5.16: *The cross section for Mueller jet in bins of $\Delta\varphi$.*

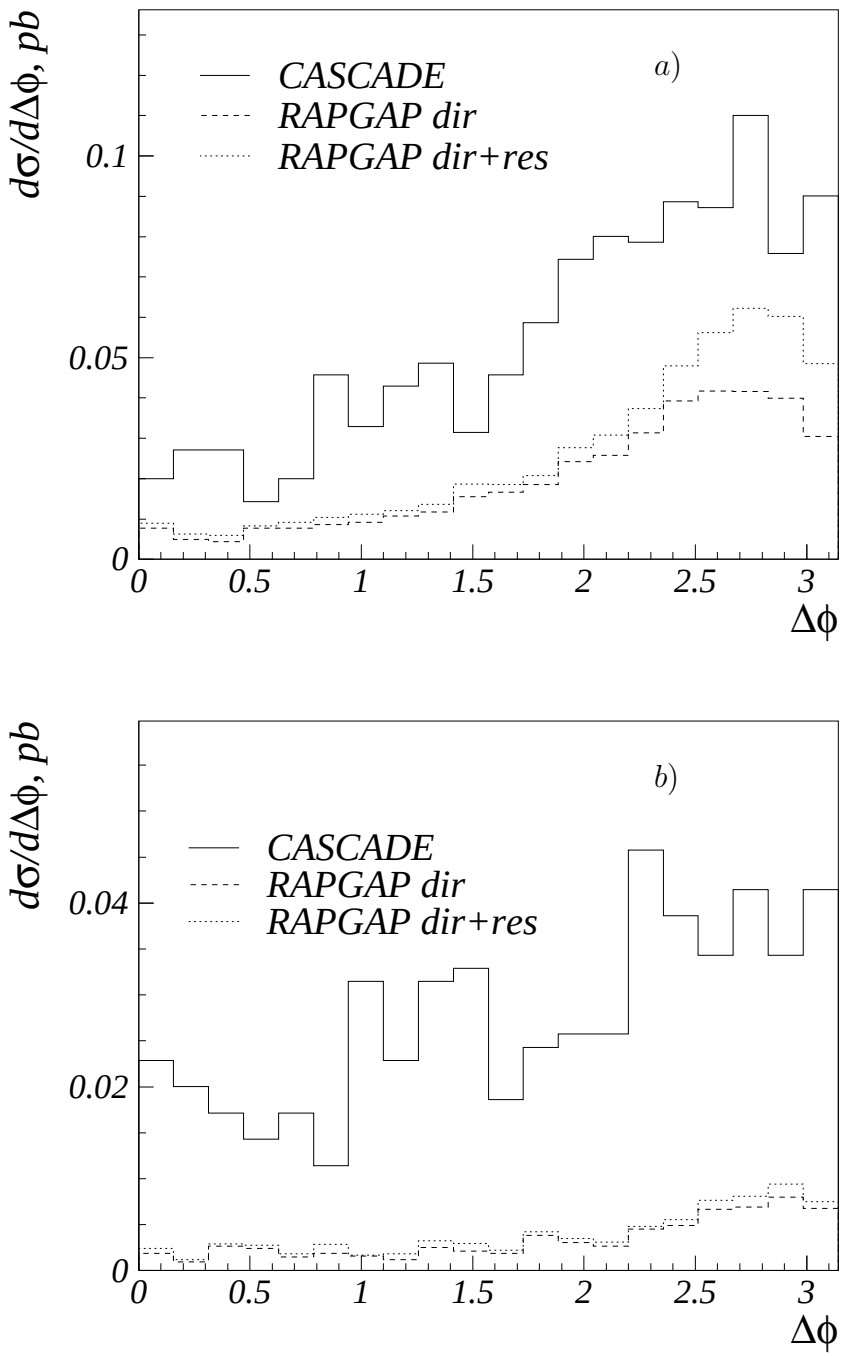

Figure 5.17: *The cross section for Mueller jet and one a) and two b) additional jets in the visible range.*

Chapter 6

Data Analysis of D* and Forward Jets

In the previous chapters results from QCD models obtained with Monte Carlo (MC) event generators were presented. In this chapter a measurement of inclusive D^* meson photoproduction and of D^* mesons associated with a forward jet is presented.

Reconstruction of D* Meson

The probability that the charm quarks fragments into a D^* meson is [6]:

$$\frac{\Gamma(c \longrightarrow D^*)}{\Gamma(c \longrightarrow anything)} = 0.255 \pm 0.017$$

The $D^{*\pm}$ meson is an excited state of the scalar meson $D^{\pm}$ and has a mass of $m(D^*) = 2010 \pm 0.5\,\mathrm{MeV}$. It has a mean life time of the order of $\tau < 10^{-24}\ s$ and it decays into a D^0 meson and a charged pion with a probability:

$$\frac{\Gamma(D^{*\pm} \longrightarrow D^0\pi^{\pm})}{\Gamma(D^{*\pm} \longrightarrow anything)} = 0.677 \pm 0.005$$

The mass difference between D^* and D^0 is very small ($m(D^*) - m(D^0) = 145.4 \pm 0.1\,\mathrm{MeV}$), which is slightly above the pion mass $m_\pi = 139.57018 \pm 0.00035\,\mathrm{MeV}$. Therefore the pion has a very small momentum and usually is called "slow" pion. The D^0 meson decays via the weak interaction through several decay channels. With a probability of (0.53 ± 0.4) the D^0 meson decays into charged kaons and another charged particles. The easiest way to reconstruct the D^* is the so-called *golden channel*, where it decays into a slow pion and charged kaon and pion– the decay products of the D^0. The golden

channel is $D^{*\pm} \longrightarrow D^0\pi_s^{\pm} \longrightarrow K^{\mp}\pi^{\pm}$. It involves three charged particles which one can measure in the tracking chambers despite its low branching ratio:

$$\begin{aligned} &\mathcal{BR}(D^{*\pm} \longrightarrow K^{\mp}\pi^{\pm}\pi_s^{\pm}) = \\ &= \mathcal{BR}(D^{*\pm} \longrightarrow D^0\pi_s^{\pm}) \cdot \mathcal{BR}(D^0 \longrightarrow K^{\mp}\pi^{\pm}) = (2.57 \pm 0.06)\% \end{aligned} \tag{6.1}$$

The decay products of the chain K, π and π_s are measured in the central tracking detectors: CJC, CIZ, COZ and CST. In each event, tracks with opposite charge are combined in pairs. To one of them the pion mass is assigned and to the second the kaon mass. The invariant mass of the pair $m(K\pi)$ is calculated and if the result is consistent with the D^0 mass, the remaining tracks with an opposite charge to that of the kaon are assigned as a slow pion. The invariant mass of the $K\pi\pi_s$ system is calculated. If the mass difference $\Delta m = m(K\pi\pi_s) - m(K\pi)$ is close to the nominal mass difference $m(D^*) - m(D^0)$ the particle is considered as a D^* candidate. It is accepted if it lies in the central region of the detector $|\eta(D^*)| < 1.5$ and has a minimum transverse momentum of at least $p_t^{D^*} > 2.\,\mathrm{GeV}$.

In order to select tracks which fit to the primary vertex the distance of closest approach was chosen to be smaller than $d'_{ca} < 2\ cm$. The cuts applied on the D^* candidates and its decay products are listed in table 6.1.

The number of D^*'s was defined by fitting the following function to the measured Δm distribution:

$$f(\Delta m) = \frac{N(D^*)}{\sqrt{2\pi}\sigma} e^{-\frac{1}{2}\frac{(\Delta m-\mu)^2}{\sigma^2}} + u_n \cdot (\Delta m - m_\pi)^{u_e} \cdot (1 - u_s(\Delta m)^2) \tag{6.2}$$

This function is the sum of a Gaussian for the signal and a background function. σ and μ present the width and the mean of the signal distributions.

Track selection (all tracks)

	Basic Cuts
p_t	$p_t > 120\ MeV$
θ	$20° \leq \theta \leq 160°$
d'_{ca}	$d'_{ca} < 2\ cm$

	Decay Products
K	$p_t^K > 0.5\ MeV$
π	$p_t^{\pi} > 0.3\ MeV$

	D^* candidate
D^0	$\lvert m(K\pi) - m(D^0)\rvert < 60\ MeV$
$p_t^{D^0}$	$p_t^{D^0} > 2\,\mathrm{GeV}$
Δm	$\Delta m < 167.5\ MeV$

Table 6.1: *Cuts applied on the tracks considered as D^* products.*

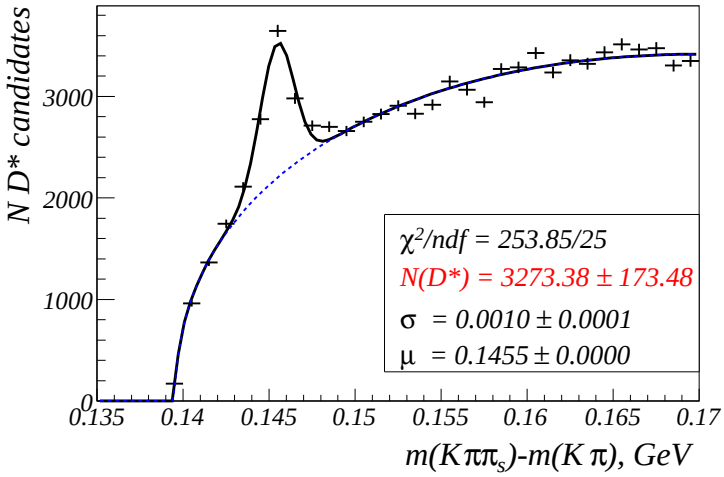

Figure 6.1: *The mass difference* Δm *between* D^0 *and* D^* *candidate.*

The background vanishes for $\Delta m \leq m_\pi$ and rises with exponent u_e (free parameter of the fit). A correction factor u_c improves the description of the distribution at high values of Δm. u_s represents the number of D^* in background.

Data Selection

The data were collected with the H1 detector in the 1999 and 2000 running period. At that time HERA was operating with electrons (positrons) with energies of $E_e = 27.6\,\text{GeV}$ and protons with an energy $E_p = 920\,\text{GeV}$. The data sample used in this analysis corresponds to a total integrated luminosity $\mathcal{L} = 59.3\ pb^{-1}$.

In order to suppress background from beam gas interactions the z–position of the vertex was chosen to be within $|z_{vtx} - z_{nom}| < 35\,\text{cm}$ around the nominal z position of the vertex.

This analysis is based on subtrigger s83, which is based on an energy deposition above threshold in the luminosity system and high p_t tracks in the tracking chambers. It requires also vertex information. Subtrigger s83 fires only if at least three tracks with momentum greater than $p_t \gtrsim 450\ MeV$ are found.

The Bjoerken variable y was reconstructed with the so-called *electron method* $y = 1 - \frac{E_{e'}}{E_e} \cdot \sin(\frac{\theta_{e'}}{2}) \approx 1 - \frac{E_{e'}}{E_e}$. It is demanded to be within $0.29 < y < 0.65$.

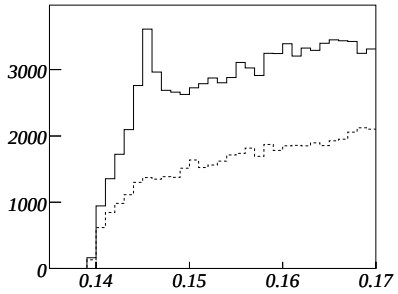

Figure 6.2: *The $\Delta m = m(K\pi\pi_s) - m(K\pi)$ distribution for the right (solid line) and for the wrong charge (dashed line) combination.*

Extracting of the Signal

In order to extract the background coming from non D^* entries in the Δm plot one can use the so–called *wrong charge* D^* candidates. Each pair of tracks with the same charge is assigned as the D^0 decay products– K and π. Afterwards it is combined with an opposite charge particle considered as the slow pion: combining $K^{\pm}\pi^{\pm}\pi_s^{\mp}$. However, the L4 trigger does not consider these wrong charge combination. Therefore they are only recorded from other independent triggers. Thus the efficiency for the wrong charge background is different than for the signal and therefore the number of the right charge combination is significantly larger.

In figure 6.2 the Δm distribution for the right charge (solid line) and for the wrong charge (dashed line) is presented. Obviously the wrong charge combination is much below the right charge. Therefore the wrong charge combinations are not used and the background is derived from the fit of equation 6.2 to the right charge combinations only. This fit is shown in figure 6.1. A signal of 3273 ± 173 D^* mesons is found.

D*+Jets Selection

In the events were a D^* candidate was found the inclusive k_t jet algorithm was applied. The jets were demanded to have minimal transverse momentum of at least $p_t^{jets} > 3.5\,\mathrm{GeV}$ in a rapidity range of $-1.5 < \eta < 2.79$. In order to extract the number of D^* when at least one jet in the visible range (as defined above) was found, the Δm fit was performed again and is shown in figure 6.3. The parameters for the fit σ, μ and u_s were fixed to the values given by the inclusive D^* sample in order to improve the fit despite the lower statistics. The total number of 2275 ± 105 D^* mesons were found together

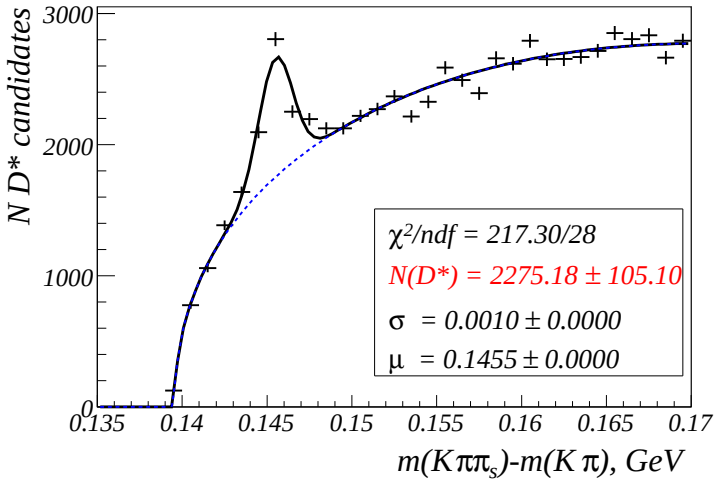

Figure 6.3: *The* Δm *distribution when at least one jet in the visible range was found.*

with jets.

In the jet and D^* sample, the Δm distribution was investigated for different rapidity ranges of the jet. These distributions can be seen in figure 6.4. In the region of $\eta^{jet} < 0$ a good D^* signal is observed. The largest amount of the D^* candidates comes from the most backward bin for η^{jet} ($-1.5 < \eta^{jet} < 0$). If the jet is more forward the number of D^* candidates becomes smaller while background increases. In the other bins the presence of the combinatorial background is very high[1], but still a D^* signal can be extracted from the fit, yielding 204 ± 37 D^* candidates if a jet is demanded in the most forward region.

Next step is to see how the Δm distribution for the most forward region looks when a different p_t^{jets} cut is applied. The Δm distribution for four different lower p_t cuts of the jets ($p_t > 2\,\text{GeV}, p_t > 4\,\text{GeV}, p_t > 4.5\,\text{GeV}$ and $p_t > 5\,\text{GeV}$) is shown in figure 6.5 for the most forward η^{jet} bin. It can be seen that for a hard p_t cut the D^* signal becomes smaller.

For large rapidity differences between the forward jet and the D^* meson there is a high probability for additional radiation between the jet and the D^*. This leads to an increase of the multiplicity which might explain the lower signal–to–background ratio.

The production of a D^* meson and forward jets was investigated. 204 ± 37

[1] *Here a forward jet has* $p_t > 3.5$ *and* $1.7 < \eta^{jet} < 2.8$. *If the additional requirements for* Mueller *jets are made* ($x_{jet} > 0.035$ *and* $0.5 < p_t^2/\mu^2 < 5$) *the* D^* *signal becomes even smaller.*

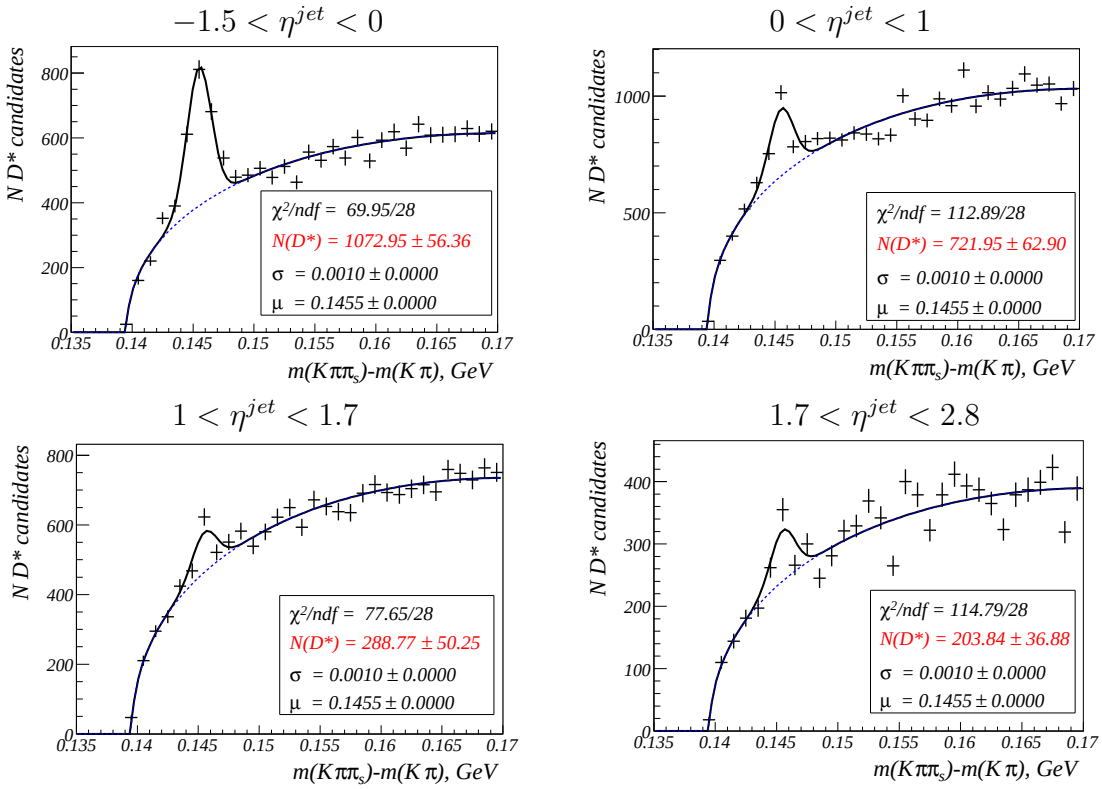

Figure 6.4: *The mass difference $m(K\pi\pi_s) - m(K\pi)$ in bins of rapidity of the jets.*

D^* mesons were found if a forward jet is required. The signal is still visible over a large background. The analysis could be improved by removing further background from the D^* signal or by increasing the statistics.The latter could be done by using untagged photoproduction which gives access to a larger phase space in y.With these improvements a measurement of D^*+forward jet is feasible and even differential cross sections, e.g as a function of $\Delta\phi$ could be measured.

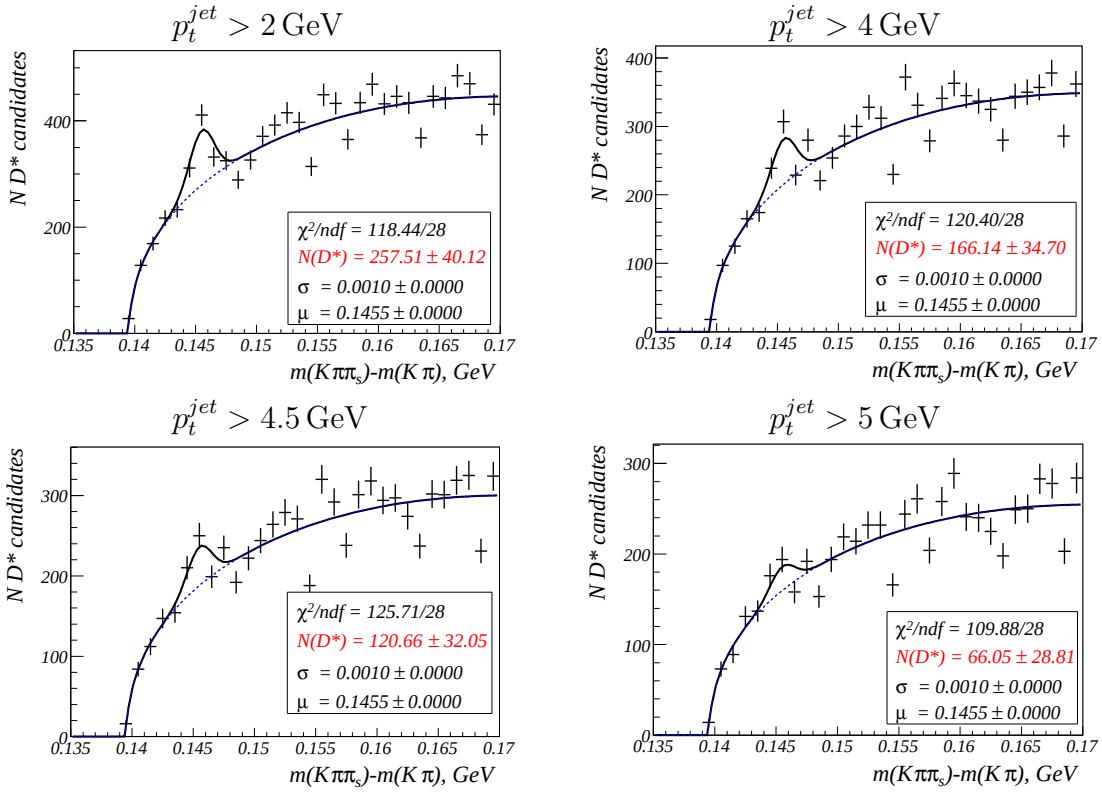

Figure 6.5: *The mass* Δm *spectra for a forward jet* $1.7 < \eta^{jet} < 2.8$ *for different cut on transverse momentum of the jet.*

Conclusions

Monte Carlo studies in deep inelastic scattering (DIS) on forward jet production in the presence of charm quarks are presented. The focus of the work is to investigate different parton evolution schemes. For this purpose the RAPGAP event generator based on DGLAP and CASCADE implementing the CCFM evolution equations are used.

For the DIS case it is shown that the charm quark mass and transverse momentum can be used as a hard scale instead of Q^2 to control phase space for parton dynamics. In this regime the scaling variable x_{Bj} is sensitive to different parton evolution schemes and it is shown that in photoproduction the hadronic final state mass W can be used. The charm quark is identified via the D^* meson. Detailed investigations of D^*+forward jet correlations are presented. It is shown that the most sensitive observables are momentum and angle correlations: $\Delta\eta$, Δp_t and $\Delta\phi$.

A first investigation of the data taken by the H1 detector in the 1999/2000 running period of HERA, corresponding to a luminosity $\mathcal{L} = 59\,\mathrm{pb}^{-1}$, with forward jets and D^* mesons is presented. Photoproduction events in a y range of $0.29 < y < 0.65$ are selected. The D^* mesons are reconstructed via the golden decay channel and 204 mesons in the presence of a forward jet are found. Although the background is large a significant signal is found.

In order to improve the measurement the statistics can be increased using the HERA II data set. The kinematic range of the analysis could be extended to higher values of y where higher values of W are accessible. Thereby the forward jet cross section increases. In addition further investigations of the cuts can be performed to improve the signal to background ratio. Also further studies of the forward jet selection could lead to an increase of the statistics without losing sensitivity to different parton evolution schemes.

The feasibility of such a measurement is important to possibly observe new effects deviating from the DGLAP evolution approach, which is the basis of the current predictions.

Appendix A

Rapidity

In the following the relation between the *rapidity* and *longitudinal momentum fraction of a parton* x is derived. For more information and detailed discussions see [19] and [20].

The light cone coordinates are defined as:

$$V^+ = \frac{V^0 + V^3}{\sqrt{2}},\ V^- = \frac{V^0 - V^3}{\sqrt{2}},\ \mathbf{V}_t = (V^1, V^2). \tag{A.1}$$

Where V^μ, $\mu = 1, 2, 3, 4$ are the components of the four vector of a particle. The scalar product of two four vectors is then defined:

$$V \cdot W = V^+ W^- + V^- W^+ - \mathbf{V}_t \cdot \mathbf{W}_t \tag{A.2}$$

$$V \cdot V = 2V^+ V^- - V_t^2 \tag{A.3}$$

A Lorenz boost in the z direction of the four vector $V^\mu \longrightarrow V'^\mu$ gives a new vector with components:

$$V'^0 = \frac{V^0 + \beta V^z}{\sqrt{1 - v^2}},\ V'^z = \frac{\beta V^0 + V^z}{\sqrt{1 - v^2}}, \tag{A.4}$$

Inserting A.4 into A.1 the same transformation performed with light cone variables appears to be:

$$V'^+ = V^+ e^\psi,\ V'^- = V^- e^{-\psi},\ \mathbf{V'_t} = \mathbf{V_t} \tag{A.5}$$

The parameter ψ is the hyperbolic angle $\psi = \frac{1}{2} \ln \frac{1+v}{1-v}$. These coordinates transform very simply under longitudinal Lorenz transformations. In addition when a particle is highly boosted along the z axis the negative component of the light cone variables vanishes while the positive one stays sizable.

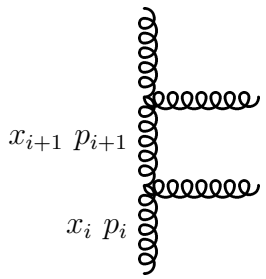

Figure A.1: *Diagram for higher order parton emission.*

A particle with mass m and a four momentum p, can be expressed in the light cone variables as:

$$p = \left(p^+, \frac{m^2}{2p^+}, \mathbf{0}_t\right) \tag{A.6}$$

The rapidity y is defined via the expression:

$$y = \frac{1}{2} \ln \frac{E + p_z}{E - p_z} \tag{A.7}$$

When using the light cone variables (A.1) this equation can be rewritten as:

$$y = \frac{1}{2} \ln \frac{p^+}{p^-} \tag{A.8}$$

With the squared four momentum $p^2 = 2p^+p^- - (\mathbf{p}_t)^2$ this can be rewritten as:

$$y = \frac{1}{2} \ln \frac{2p^+p^+}{p^2 + p_t^2} \tag{A.9}$$

For virtual particles the denominator of the fraction in equation (A.9) can become smaller than zero where the logarithm is not defined. The rapidity of a virtual particle is therefore defined:

$$y = \ln \frac{p^+}{p_t} \tag{A.10}$$

The momentum can be expressed with $p = (p^+, p^-, \mathbf{p}_t) = (k^+x^+, k^-x^-, \mathbf{p}_t)$ where x denotes the fractional momentum (see figure A.1). Then equation (A.10) becomes:

$$y = \ln \frac{x^+k^+}{p_t} = \ln x^+ + \ln \frac{k^+}{p_t}, \tag{A.11}$$

which finally leads to proportionality between the longitudinal momentum fraction and the rapidity since $\ln(k^+/p_t)$ is constant for fixed p_t:

$$y \backsim \ln x^+ \tag{A.12}$$

Bibliography

[1] J. D. Bjoerken and E. A. Paschos, *Inelastic electron proton and gamma proton scattering, and the structure of the nucleon*, Phys. Rev. **185** (1969), 1975.

[2] A. Pich, *Quantum chromodynamics* (1995), `hep-ph/9505231`.

[3] D. Perkins, *Introduction to High Energy Physics, 4th Edition*, Cambridge University Press (2004).

[4] R. Devenish and A. Cooper-Sarkar, oxford, UK: Univ. Pr. (2004) 403 p.

[5] H. Jung, *What is CCFM, Why k_t-factorization? Why and how all that?*, URL `http://sesam.desy.de/seminar/jung.ps.gz`.

[6] S. Eidelman et al. (Particle Data Group Collaboration), *Review of particle physics*, Phys. Lett. **B592** (2004), 1.

[7] M. Karlsson, *A Study of Parton Dynamics from Deep Inelastic Scattering Events Containing a Jet in the Forward Direction*, Ph.D. thesis, University of Lund (2002).

[8] G. Flucke, *Photoproduction of D^* meson and D^* associated with jets at HERA*, Ph.D. thesis, University of Hamburg (2005).

[9] H. Jung, *Hard diffractive scattering in high-energy e p collisions and the Monte Carlo generation RAPGAP*, Comp. Phys. Commun. **86** (1995), 147.

[10] H. Jung and G. P. Salam, *Hadronic final state predictions from CCFM: The hadron- level Monte Carlo generator CASCADE*, Eur. Phys. J. **C19** (2001), 351, `hep-ph/0012143`.

[11] S. V. Chekanov, *Jet algorithms: A mini review* (2002), `hep-ph/0211298`.

[12] S. D. Ellis and D. E. Soper, *Successive combination jet algorithm for hadron collisions*, Phys. Rev. **D48** (1993), 3160, hep-ph/9305266.

[13] I. Abt et al. (H1 Collaboration), *The H1 detector at HERA*, Nucl. Instrum. Meth. **A386** (1997), 310.

[14] I. Abt et al. (H1 Collaboration), *The Tracking, calorimeter and muon detectors of the H1 experiment at HERA*, Nucl. Instrum. Meth. **A386** (1997), 348.

[15] A. H. Mueller, *Jets at LEP and HERA*, J. Phys. **G17** (1991), 1443.

[16] C. Adloff et al. (H1 Collaboration), *Forward jet and particle production at HERA*, Nucl. Phys. **B538** (1999), 3, hep-ex/9809028.

[17] A. Aktas et al. (H1 Collaboration), *Forward jet production in deep inelastic scattering at HERA*, Eur. Phys. J. **C46** (2006), 27, hep-ex/0508055.

[18] H. Jung, L. Jonsson, and H. Kuster, *The role of resolved virtual photons in the production of forward jets at HERA*, Eur. Phys. J. **C9** (1999), 383, hep-ph/9903306.

[19] J. C. Collins, *Light-cone variables, rapidity and all that* (1997), hep-ph/9705393.

[20] H. Jung Lectures given at the Hamburg Univercity in the Winter semester of 2005.

Acknowledgements

Here I am :) Although it took me some time to finalize the work it is done! And here comes the place to express my gratitude to the many people surrounding me during the last months. And here they are:

To Prof. Jordan Stamenov and Dr. Ivan Tsakov from the Institute for Nuclear Research and Nuclear Energy of Bulgarian Academy of Science. Thank you for your support and the possibility to perform the present work.

Of course I can not forget to thank Dr. Max Klein for all the help and trust in me. It is a great pleasure for me just to say *Thank you.*

Special thanks go to my supervisor, Dr. Hannes Jung, who taught me and inspired me during the whole two years we have been working together. For the encouragement and the patience, for the conversations about what is beyond.

To Prof. Beate Naroska for the interest in my thesis, to Dr. Carsten Niebuhr for the support.

To Christiane Risler for the careful reading of the work, for her friendship and for the makaroni.

To my officemates– Nina, Axel, Lluis and Tobias for the nice atmosphere in the office although sometimes it becomes too hot...

To Angela for the *objects* and to Kaloyan for the *orientation.* Without their help I have no idea how I would manage.

To all my colleagues from H1 for answers even when it was difficult to understand the question...

To my parents and my relatives, for what I am. Especially to my brother– Lazar and his wife Margarita for the nice weekends and their friendship.

To all my friends here and everywhere. To Kaloyan, Sasha, Dirk and Stine, Kalina, Vikt., Mira, Iva (both), Mera, Vesela, ludDido, Nevena, Galia...

It is always hard to express your gratitude such a way to sound nice especially to your closest friend. Therefore I just say *Thank you*, Kalo, for your useful words about physics and problems, support and friendship!